



HAL
open science

Evidence of an Ozone Mini-Hole Structure in the Early Hunga Tonga Plume Above the Indian Ocean

Tristan Millet, Hassan Bencherif, Thierry Portafaix, Nelson Bègue, Alexandre Baron, Valentin Duflot, Michaël Sicard, Jean-Marc Metzger, Guillaume Payen, Nicolas Marquestaut, et al.

► **To cite this version:**

Tristan Millet, Hassan Bencherif, Thierry Portafaix, Nelson Bègue, Alexandre Baron, et al.. Evidence of an Ozone Mini-Hole Structure in the Early Hunga Tonga Plume Above the Indian Ocean. Atmospheric Chemistry and Physics Discussions, 2024, 10.5194/egusphere-2023-2645 . insu-04301019

HAL Id: insu-04301019

<https://insu.hal.science/insu-04301019>

Submitted on 22 Nov 2023

HAL is a multi-disciplinary open access archive for the deposit and dissemination of scientific research documents, whether they are published or not. The documents may come from teaching and research institutions in France or abroad, or from public or private research centers.

L'archive ouverte pluridisciplinaire **HAL**, est destinée au dépôt et à la diffusion de documents scientifiques de niveau recherche, publiés ou non, émanant des établissements d'enseignement et de recherche français ou étrangers, des laboratoires publics ou privés.



Distributed under a Creative Commons Attribution 4.0 International License



Evidence of an Ozone Mini-Hole Structure in the Early Hunga Tonga Plume Above the Indian Ocean

Tristan Millet¹, Hassan Bencherif¹, Thierry Portafaix¹, Nelson Bègue¹, Alexandre Baron², Valentin Duflot¹, Michaël Sicard^{1,3}, Jean-Marc Metzger⁴, Guillaume Payen⁴, Nicolas Marquestaut⁴, and Sophie Godin-Beekmann⁵

¹LACy, Laboratoire de l'Atmosphère et des Cyclones, UMR 8105 CNRS, Université de La Réunion, Météo-France, 97744 Saint-Denis, France

²Cooperative Institute for Research in Environmental Sciences, and NOAA Chemical Sciences Laboratory, Boulder, USA

³CommSensLab-UPC, Universitat Politècnica de Catalunya, Barcelona, Spain

⁴Observatoire des Sciences de l'Univers de La Réunion (OSUR), CNRS/Université de La Réunion/Météo-France, UAR 3365, Saint-Denis, France

⁵Laboratoire Atmosphère Milieux Observations Spatiales, LATMOS-IPSL, UMR 8190, Sorbonne Université - UVSQ - CNRS, Paris, France

Correspondence: Tristan Millet (tristan.millet@univ-reunion.fr)

Abstract. On 15 January 2022, the Hunga Tonga-Hunga Ha'apai (HTHH) volcano (20.5° S, 175.4° E) erupted, releasing significant amounts of aerosols, sulfur dioxide (SO₂), and water vapor (H₂O) into the stratosphere. Due to the general stratospheric circulation of the southern hemisphere, this volcanic plume traveled westward and impacted the Indian Ocean and Reunion (21.1° S, 55.5° E) a few days after the eruption. This study aims to show how the currently available ozone observations highlight the stratospheric dynamics during the first week following the eruption. The Ozone Mapping and Profiler Suite Limb Profiler (OMPS-LP) aerosol extinction profiles were used to investigate the vertical and latitudinal extension of the volcanic plume over the Indian Ocean. The volcanic aerosol plume was also observed with an aerosol lidar and a sun-photometer located at Reunion. The impact of this plume on stratospheric ozone was then investigated using MLS (Microwave Limb Spectrometer), OMI (Ozone Monitoring Instrument), MERRA-2 (Modern-Era Retrospective analysis for Research and Applications, version 2) and M2-SCREAM (MERRA-2 Stratospheric Composition Reanalysis of Aura MLS) ozone profiles and total ozone. The results show that the volcanic plume traveled over Reunion at altitudes ranging from 26.8 to 29.7 km and spanned more than 20 degrees of latitude over the Indian Ocean. Ozone analyses reveal an ozone mini-hole structure, with the Total Column Ozone (TCO) anomaly of -15 DU from MERRA-2 covering an area of 12.06×10⁵ km² on 17 January and 4.94 ×10⁵ km² on 22 January. The ozone profiles from MLS show that a maximum stratospheric column ozone anomaly of -14.66 DU (-6.38 %) was found within the aerosol plume on 20 January.

1 Introduction

Due to its high oxidizing potential and contribution to the radiative budget, ozone plays an undeniable role in the Earth's atmosphere (IPCC, 2013; Organization, 2018; IPCC, 2021). In the stratosphere, ozone serves as a protective shield for the



20 biosphere by absorbing the majority of solar ultraviolet radiation (UVR) in the 280–315 nm range. This shielding action
protects human health and ecosystems from the harmful effects of UV-B radiation, which can lead to adverse health issues such
as cataracts, melanoma, and skin aging, while deteriorating materials (Pitts et al., 1977; Matsumura and Ananthaswamy, 2004;
Bernhard et al., 2020). In the past decades, anthropogenic emission of chlorofluorocarbons (CFCs) was responsible for the rapid
decline in stratospheric ozone (Rowland, 1996). Within the stratosphere, CFCs are photo-dissociated into chlorine compounds
which are known to efficiently deplete ozone (Solomon, 1999). Following the ratification of the Montreal Protocol in 1987,
25 CFC emissions were gradually restricted, and previous research and reports show that the ozone layer is expected to return to
its 1980s levels from the middle to the end of the century, depending on the latitude (Dhomse et al., 2018; Organization, 2018).
On the other hand, tropospheric ozone is a secondary pollutant that directly harms ecosystems, reduces crop productivity, and
has negative effects on human health (Mills et al., 2018; Nuvolone et al., 2018). Photochemical formation of tropospheric
ozone is driven by the combination of solar radiation and ozone precursors, including Volatile Organic Compounds (VOCs),
30 nitrogen oxides (NO_x) and aerosols (Jacob, 1999; Ivatt et al., 2022). Ozone in the troposphere can therefore be enhanced by
anthropogenic activities such as agriculture, industry and transport, that release nitrogen oxides and aerosols.

Besides, stratospheric air-masses can break through the tropopause and penetrate the troposphere in events described as
stratosphere-to-troposphere exchanges (Holton et al., 1995). These exchanges can significantly enhance ozone levels within
the whole free troposphere (Clain et al., 2010). Following emissions from biomass fires, ozone precursors can also produce
35 tropospheric ozone (Andreae and Merlet, 2001; Jaffe and Wigder, 2012). Biomass burning indeed results in the production of
carbon monoxide (CO), which, when oxidized by the hydroxyl radical (OH), can lead to ozone formation in the surrounding
areas (Randriambelo et al., 2000). However, when the fire is intense, ozone precursors can be ejected above the planetary
boundary layer where stronger winds can carry them over much greater distances, resulting in ozone pollution events far from
the biomass burning region (Baldy et al., 1996). As such, because Reunion is situated at the intersection of austral winter
40 atmospheric flows, it is regularly under the influence of air-masses with ozone precursors from Madagascar, Southern Africa
and Southern America, but studies have also shown that it is sometimes affected by advection from Australia and South-Eastern
Asia (Baldy et al., 1996; Randriambelo et al., 2000; Dufflot et al., 2010; Bègue et al., 2010; Dufflot et al., 2011; Vigouroux et al.,
2012; Bencherif et al., 2020; Ranaivombola et al., 2023).

Additionally, explosive volcanic eruptions can influence both stratospheric and tropospheric ozone concentrations, and thus
45 play a role in global chemistry and radiative forcing (Robock, 2000). Previous major eruptions, such as that of Mount Pinatubo
(1991) and El Chichón (1982) have had significant effects on global atmospheric chemistry that are well documented (Hofmann
and Solomon, 1989; Gobbi et al., 1992; McCormick et al., 1995; Organization, 1999; Guo et al., 2004). Indeed, major explosive
eruptions generally eject enormous quantities of aerosols and sulfur dioxide (SO₂) which can alter ozone chemistry. The
primary effect of volcanic aerosols on ozone is associated with the activation of chlorine compounds on volcanic particles.
50 When SO₂ is released during eruptions, it undergoes rapid transformation into sulfuric acid (H₂SO₄) particles which can
contribute to the depletion of ozone. For instance, McCormick et al. (1995) reported that tropical column ozone decreased by
6–8 % in the months following the Mount Pinatubo eruption. They observed that losses were greatest below 28 km, amounting
to 20 % in the 24–25 km altitude range (McCormick et al., 1995). Moreover, as stated by Hofmann and Solomon (1989),

reactive anthropogenic chlorine compounds may be enhanced in volcanically perturbed regions, leading to ozone depletion
55 (Hofmann and Solomon, 1989).

Because of the implied ozone losses and radiative forcing anomalies, the injection of volcanic plumes into the stratosphere can also influence atmospheric temperatures. Ramaswamy et al. (2006) observed increases in global lower stratosphere temperatures following the major eruptions of El Chichón and Mount Pinatubo (Ramaswamy et al., 2006). It was also found that the ozone depletion in the aerosol layer caused by the Mount Pinatubo eruption reduced the stratospheric heating by 30 % (Kirchner et al., 1999). Nonetheless, the corresponding radiative anomalies caused global stratospheric warming and tropospheric cooling (Stenchikov et al., 1998; Kirchner et al., 1999).

Moderate and major eruptions may also contribute to the amplitude and dimension of the ozone hole over Antarctica. Following the Mount Pinatubo eruption, Hofmann and Oltmans (1993) observed unusually low total ozone values of 105 DU over the South Pole Station, which they attributed to the enhancement of Polar Stratospheric Clouds (PSCs) volume that play
65 an important role on ozone depletion process due to the presence of sulfuric acid droplets (Hofmann and Oltmans, 1993). Ivy et al. (2017) reported an increase of the 2015 Antarctic ozone hole by 4.5×10^6 km², primarily attributed to volcanic aerosols from the Calbuco eruption (Ivy et al., 2017). Similarly, Zhu et al. (2018) reported volcanic sulfate aerosols penetration from the Calbuco eruption into the Antarctic polar vortex, resulting in earlier ozone loss and an increase in the area of the ozone hole (Zhu et al., 2018). Yook et al. (2022) also hypothesized a link between the eruption of La Soufrière in 2021 and the longevity
70 of the 2021 ozone hole (Yook et al., 2022). Hence, numerous research papers focused on ozone chemistry and atmospheric forcings following eruption events.

This study focuses on the January 2022 Hunga Tonga-Hunga Ha'apai (HTHH) eruption with a particular emphasis on the ozone-related data in the week following the eruption. This eruption can be regarded as the most powerful since the eruption of Mount Pinatubo three decades ago. Its consequences have been under intensive scrutiny and studies reveal this eruption
75 injected ~ 0.5 Tg of SO₂ and 146 ± 5 Tg of water vapor (H₂O) into the stratosphere, corresponding to an increase of ~ 10 % of the global stratospheric water vapor burden (Sellitto et al., 2022; Zuo et al., 2022; Millán et al., 2022). Research has also shown that the main eruption's aerosol column extended through the troposphere and stratosphere, and even reached the lower mesosphere (Carr et al., 2022). As a result of the main austral summer stratospheric circulation, the bulk of the HTHH aerosol plume reached the Indian Ocean and Reunion just 4 days after the main eruption (Baron et al., 2023). Studies pointed out
80 that the stratospheric volcanic plume caused a stratospheric cooling during the first two weeks following the eruption, since water vapor radiative cooling dominated local stratospheric heating rates (Sellitto et al., 2022; Legras et al., 2022; Wang et al., 2022). The dilution and dispersion of the water vapor and aerosol plume lead to a net warming of the climate system and persisting low temperatures within the stratosphere (Sellitto et al., 2022; Coy et al., 2022). Jenkins et al. (2023) indicated that the stratospheric water vapor perturbation brought by the HTHH could increase the global surface temperature in the coming
85 decade (Jenkins et al., 2023).

The present paper describes the currently available observations from the Microwave Limb Sounder (MLS), the Ozone Monitoring Instrument (OMI), as well as assimilated fields from Modern-Era Retrospective analysis for Research and Applications, version 2 (MERRA-2) and MERRA-2 Stratospheric Composition Reanalysis of Aura MLS (M2-SCREAM) (Gelaro et al.,



2017; Wargan et al., 2023). Care must be taken with the interpretation of early ozone results due to the impact of volcanic
90 aerosols on satellite UV/visible observations, which significantly affects ozone OMI measurements. As OMI observations are
assimilated into MERRA-2 and M2-SCREAM, the analyses may also be influenced by instrumental bias. Given the large per-
turbations caused by the volcanic plume and the limitations of satellite data and assimilation techniques, rather than trying to
be quantitative on the ozone perturbation, we will use these observations to qualitatively assess the stratospheric dynamics at
stake in the early volcanic plume. Hence, the objective of the present manuscript can be summarized in two main points: firstly,
95 we describe the currently available observations and demonstrate the appearance of a structure resembling an ozone mini-hole;
and secondly, we show the zonal displacement of the volcanic aerosol plume and the dynamics of its advection with the help
of the ozone data.

This article is organized as follows: Sect. 2 describes the instruments and observations that were used for the present study,
as well as the data processing and methodology. Section 3 presents the results regarding the volcanic aerosol plume, the ozone
100 data over the Indian Ocean as well as the dynamics of the advection. Section 4 is dedicated to a discussion on the ozone results.
Finally, the conclusion in Sect. 5 summarizes the results of this research.

2 Instrumentation and Method

In this study, we combined ground-based and satellite observational data, both before and after the HTHH eruption, along with
numerical assimilation data. This section outlines the different types of ozone and aerosol data used.

105 2.1 Ozone measurements

A stratospheric Differential Absorption Lidar (DIAL) has been operated since January 2013 at the Maïdo Observatory (2160
m asl) of Reunion (Baray et al., 2013; Portafaix et al., 2015). Lidar observations have the advantage of providing high temporal
and vertical resolutions (Pazmiño, 2006)), with an accuracy of $\sim 5\%$ below 20 km, $\sim 3\%$ in the 20–30 km altitude range and
15–30% above 45 km (Godin-Beekmann et al., 2003). This instrument can retrieve ozone concentration profiles at altitudes
110 ranging from 15 to 45 km. However, although the Maïdo DIAL system recorded data during the initial passage of the volcanic
plume in January 2022, the corresponding signal-to-noise ratio was extremely low and the ozone profiles were not relevant. As
a result, stratospheric DIAL ozone profiles used in this paper were recorded before the HTHH eruption, from January 2013 to
December 2021. The 470 ozone profiles obtained during this period were used to determine the background ozone level and
were compared with satellite and assimilation products. As part of the Network for the Detection of Atmospheric Composition
115 Change (NDACC), this data can be accessed at the following link: <https://ndacc.larc.nasa.gov/> (last accessed on 23 August
2023).

Ozone profiles and Total Column Ozone (TCO) data can be retrieved from satellite measurements. In comparison to ground-
based observations, satellite measurements offer a global coverage and a consistent measurement frequency. The MLS in-
strument is a spectrometer on the Aura satellite, launched in July 2004 along with OMI. The Aura satellite follows a helio-
120 synchronous orbit and passes the equator at 01:45 pm solar time on its ascending node. In order to calculate atmospheric



parameters like temperature and atmospheric component concentrations, MLS measures thermal radiation emitted from the Earth's atmospheric limb ahead of its orbital path at spectral wavelengths ranging from 0.12 to 2.5 mm (Waters et al., 2006; Livesey et al., 2008). According to Millán et al. (2022) who used level 2 version 4 MLS data following the HTHH eruption, similar but spurious features are seen in many of the MLS retrieved species because of interference from SO₂ absorption lines (Millán et al., 2022). However, the quality of ozone and temperature measurements are not affected by the aerosol plume (Millán et al., 2022). Here, ozone concentration profiles with respect to geometric altitude were constructed with MLS level 2 version 5 ozone volume mixing ratio, temperature and geopotential profiles (Livesey et al., 2022). To fit with the lidar time series, this procedure was repeated for both ascending and descending nodes on each measuring day from January 2013 to December 2021. This procedure was extended to January 2022 in order to include MLS ozone profiles recorded before and after the HTHH eruption. To calculate Stratospheric Column Ozone (SCO) data from MLS over the Indian Ocean, all available ozone concentration profiles within a 5-degree radius were averaged. In most of the stratosphere, specifically between 1 hPa and 68 hPa, ozone volume mixing ratio profiles have accuracy and precision that are both lower than 10 % (Livesey et al., 2022). In accordance with the recommendations made in the MLS data quality and description document, all quality flags (quality, convergence, status and precision) were used on the raw profiles, and data lying outside the recommended range (261 to 0.001 hPa, or approximately 11 to 90 km) were not used (Livesey et al., 2022). MLS observations can be accessed through NASA's data portal (<https://disc.gsfc.nasa.gov/>, last accessed on 23 August 2023).

On the other hand, OMI observes the atmosphere at nadir and uses a UV/visible spectrometer combined with a wide-field telescope (Levelt et al., 2006, 2018). The main goal of OMI is to continue the Total Ozone Mapping Spectrometer (TOMS) mission which was to monitor total ozone and other atmospheric parameters related to ozone chemistry. Thus, we have used TCO (TOMS-like) level 3 data from the OMTO3e product consisting in best quality filtered level 2 TCO data re-arranged on a regular spatial grid of 0.25°×0.25° (OMI team, 2012). OMI level 2 ozone data has a precision of ~3 % and shows good agreement with Dobson and SAOZ measurements over the southern tropics and subtropics (Toihir et al., 2018). Because OMI observes in the UV/visible spectral range, its ozone measurements are found to be particularly influenced by the large quantity of stratospheric aerosol and SO₂. It is important to note that the OMI processing algorithm is not designed to handle such high levels of stratospheric aerosols. Taha et al. (2022) indeed found that the measured stratospheric Aerosol Optical Depth (sAOD) for this event is more than double that for the 2015 Calbuco eruption, underlying the severity of this eruption (Taha et al., 2022). In fact, filtering level 2 OMI data for 17 January effectively removes the majority of the anomalous data points. Consequently, instead of using OMI to quantify the ozone loss or anomaly, we use its ozone data solely to track the location of the ozone anomaly and to discuss currently available products which assimilate OMI measurements. OMI data can be accessed using NASA's data portal (<https://disc.gsfc.nasa.gov/>, last accessed on 23 August 2023).

Assimilation products have the ability to estimate atmospheric parameters with high temporal and spatial resolutions by combining observational information from multiple sources and propagating it forward in time using fundamental laws of motion. Modern-Era Retrospective analysis for Research and Applications, version 2 (MERRA-2), created by NASA's Global Modeling and Assimilation Office (GMAO), is such an assimilation dataset which analyses numerous atmospheric parameters from 1980 to the present (Koster et al., 2016; Wargan et al., 2017). Since the launch of the Aura satellite in 2004, ozone profiles



from MLS and TCO from OMI have been used exclusively in the assimilation of MERRA-2 ozone profiles and TCO fields (Table 1 of (Wargan et al., 2017)). In order to fit with the lidar time series and to study the effects of the HTHH volcanic plume on ozone variability, we used MERRA-2 3-hourly ozone profiles from the M2I3NVASM v5.12.4 product for the study period (i.e. from January 2013 to January 2022) (Global Modeling and Assimilation Office (GMAO), 2015a). These profiles were downloaded over all grid points covering the Indian Ocean, from (30.0° S, 40.0° E) to (0.0° S, 175.0° E). To study the impact of the volcanic plume on TCO, we also downloaded MERRA-2 total ozone distributions from the M2I1NXASM v5.12.4 product over the same time period (January 2013 to January 2022) and over the same region (Global Modeling and Assimilation Office (GMAO), 2015b). Both datasets share a $0.5^\circ \times 0.625^\circ$ latitude and longitude resolution, but they are sampled on slightly different temporal grids. Ozone profiles from the M2I3NVASM v5.12.4 are recovered 3-hourly from 00:00 UTC and TCO maps from the M2I1NXASM v5.12.4 product are recovered hourly from 00:00 UTC. In a comparison with Upper Atmosphere Research Satellite (UARS) MLS, Michelson Interferometer for Passive Atmospheric Sounding (MIPAS) and Stratospheric Aerosol and Gas Experiment II (SAGE II) data, Wargan et al. (2017) found that global MERRA-2 ozone profiles show differences of less than 10 %, except at high latitudes (Wargan et al., 2017). They also found that global MERRA-2 TCO data show differences lower than 2 % in comparison with TOMS data. Overall, they reported MERRA-2 stratospheric ozone variability to be well represented, and justified its use for studies requiring highly resolved ozone acquisitions. MERRA-2 data can be accessed using NASA's data portal (<https://disc.gsfc.nasa.gov/>, last accessed on 23 August 2023). We also utilized ozone profiles from the European Centre for Medium Range Forecasts (ECMWF) ERA5 reanalyses. These ozone profiles were obtained hourly on 137 model levels and have a $0.25^\circ \times 0.25^\circ$ resolution. By comparing MERRA-2 and ERA5 ozone profiles with the DIAL profiles, we determined which assimilation product displayed the closest agreements with local remote sensing measurements. The selected assimilation profiles for Reunion (where the DIAL instrument is located) from MERRA-2, and ERA5 are chosen from the grid point nearest to Reunion. Data from ERA5 can be obtained from ECMWF's Climate Data Store (<https://cds.climate.copernicus.eu/#!/home>, last accessed on 23 August 2023).

Additionally, we used MERRA-2 Stratospheric Composition Reanalysis of Aura MLS (M2-SCREAM) profiles following the eruption over the aforementioned region. M2-SCREAM distinguishes itself from MERRA-2 by also assimilating water vapor and chemical species data obtained from MLS, integrating them into a complete stratospheric chemistry model called StratChem (Wargan et al., 2023; Nielsen et al., 2017). Coy et al. (2022) employed M2-SCREAM's water vapor profiles in the context of the HTHH eruption and concluded that M2-SCREAM effectively represents the water vapor anomaly from the eruption and accurately captures the stratospheric dynamics (Coy et al., 2022). M2-SCREAM data can be downloaded through this link: <https://disc.gsfc.nasa.gov/datasets?keywords=M2-SCREAM&page=1> (last accessed on 23 August 2023).

To investigate ozone profiles over the Indian Ocean, we used ozone profiles from the M2I3NVASM v5.12.4 dataset to derive TCO and SCO. In order to determine the SCO, one needs to detect the tropopause height. Following the method reported by Bencherif et al. (2020) and by Sivakumar et al. (2011), we used the Lapse Rate Tropopause (LRT) height (Bencherif et al., 2020; Sivakumar et al., 2011). The LRT is detected as the lowest height at which the temperature gradient is greater than -2K/km and the average temperature gradient of the next 2 km also exceeds -2K/km . The SCO is then calculated by integrating



190 the ozone concentration profile between the LRT and the stratopause heights. In this work, the stratopause height was estimated to be at 47.5 km.

2.2 Aerosol measurements

In addition to the DIAL system, the Reunion atmospheric observatory is equipped with several other active remote sensing systems, including a Rayleigh-Mie lidar for aerosol profile measurements (Baron et al., 2023). In this study we used aerosol
195 extinction profiles together with the corresponding sAOD at 532 nm as derived from the Rayleigh-Mie lidar measurements at the Reunion observatory. The data used in this study are publicly accessible via this webpage: <https://geosur.osureunion.fr/geonetwork/srv/eng/catalog.search#/metadata/f2c35798-47b7-433c-8927-46cf7babca83>. The L2 ready-to-use data set in netCDF format are available through this link: <https://doi.org/10.5281/zenodo.7790283> (last accessed on 14 September 2023).

Aerosol optical properties can also be retrieved using sun-photometers. These remote sensing sun-tracking radiometers
200 perform regular and frequent measurements of the direct solar spectral irradiance, typically at wavelengths between 340 nm and 1640 nm. By comparing the ground solar irradiance to the estimated top of the atmosphere irradiance, they can determine the total Aerosol Optical Depth (AOD), a quantity that describes the opacity of the atmosphere to radiation. Therefore, a sun-photometer gives a measure of aerosol abundance in the atmospheric column above the study site. In the present study, we used AOD data from a Cimel sun-photometer located in Saint-Denis campus (20 km northeast of the observatory at 80 m asl),
205 which has been operating since December 2003 in the framework of the AERONET (AERosol RObotic NETwork) program. We used version 3 level 2.0 AERONET data for the period from December 2003 to January 2022. AERONET data of level 2.0 is quality-controlled with near-real time automatic cloud-screening in addition to having pre- and post-field calibrations. According to Giles et al. (2019), the 1σ uncertainty for the near-real time AERONET AOD measurement is up to 0.02 (Giles et al., 2019). AERONET data are accessible from <https://aeronet.gsfc.nasa.gov/> (last accessed on 23 August 2023).

210 The Ozone Mapping and Profiler Suite Limb Profiler (OMPS-LP) monitors the Earth limb ahead of its orbit path to provide high vertical resolution ozone and aerosol profiles. The instrument measures limb scattering radiances in the 290–1000 nm wavelength range over the sunlit portion of the atmosphere using three vertical slits. This instrument has been making observations onboard the Suomi National Polar-orbiting Partnership (Suomi NPP) spacecraft since January 2012, following a helio-synchronous orbit with an equatorial passing time of 01:30 pm solar time on its ascending node. With the goal to study
215 the spatial extension of the plume, we used OMPS-LP aerosol extinction profiles at 745 nm. According to Taha et al. (2021), extinction coefficients at 745 nm have relative accuracy and precision of 10 % and 15 %, respectively (Taha et al., 2021). OMPS data were downloaded from the following link: <https://ozoneaq.gsfc.nasa.gov/> (last accessed on 23 August 2023).

2.3 Stratospheric dynamics

To investigate the origin of the air-masses in our study region, we used the HYbrid Single Particle Lagrangian Integrated
220 Trajectory (HYSPLIT) model in its passive and backward mode. Developed by the National Oceanic and Atmospheric Administration (NOAA), this model uses meteorological fields to compute and simulate trajectories of air-masses (Draxler and Hess, 1997, 1998). Because the long-lasting HTHH atmospheric effects appear to be concentrated within the stratosphere, and



since stratospheric circulation is stable and stratified, we used a single HYSPLIT simulation to highlight the trajectories of air-masses in the stratosphere over the Indian Ocean (Sellitto et al., 2022; Zuo et al., 2022; Millán et al., 2022). Thus, using
225 meteorological fields from the Global Data Assimilation System (GDAS), we ran a 240 hours back-trajectory simulation of
9 distinct air parcels with terminal altitudes distributed equitably between 22 and 26 km (National Oceanic and Atmospheric
Administration (NOAA), 2023). These trajectories were chosen to have their endpoint where the impact of the volcanic plume
on TCO appears to be the greatest in the western region of the Indian Ocean. HYSPLIT trajectories can be obtained by running
simulations through the following link: https://www.ready.noaa.gov/HYSPLIT_traj.php (last accessed on 23 August 2023).

230 To investigate the dynamics of the stratosphere during the advection of the volcanic plume, we also used ERA5 analyses
of Ertel's Potential Vorticity (EPV) at the 600 K isentropic level (~24 km in altitude) for the period from 18 to 24 January,
in conjunction with MERRA-2 and GDAS data (utilized for driving HYSPLIT). This integration of data from diverse sources
enhances the robustness of our analysis and provides a valuable approach to assess uncertainties and ensure consistency.
According to Hoskins et al. (1985), the EPV on isentropic surfaces behaves as a dynamical tracer when diabatic effects are
absent (Hoskins et al., 1985). Many authors have demonstrated its utility in studying isentropic transport in the stratosphere
235 (Holton et al., 1995; Bencherif et al., 2003; Semane et al., 2006; Bencherif et al., 2011). EPV maps on the 600 K isentropic
level were downloaded from ECMWF's data archive (MARS) using a CDS API key.

EPV maps over the study area were analysed further using the DYnamical Barrier Localization (DYBAL) algorithm, which
allows the localization of the subtropical barrier. The DYBAL code is a numerical tool developed at the Laboratoire de
240 l'Atmosphère et des Cyclones (LACy, France) to detect dynamical barriers and mixing in the subtropical stratosphere (Portafox
et al., 2003). The detection of a dynamical barrier is based the EPV gradient in equivalent latitude coordinates as defined by
Nakamura (1996), with its position characterized by a local maximum of the EPV gradient (Nakamura, 1996; Manney et al.,
2022, 2023). Here we applied the DYBAL code to maps extracted from the ERA5 EPV fields on the 600 K isentropic surface.
The ability of DYBAL to detect the position and the deformation of the dynamical barriers was previously highlighted by
245 several authors (Portafox et al., 2003; Morel et al., 2005; Bencherif et al., 2007).

2.4 Inter-comparison

Prior to drawing any conclusions based on the MLS and assimilated ozone concentration profiles, it is essential to verify their
agreement with precise local observations, such as lidar observations. For the purpose of this inter-comparison process, only
the ozone profiles that show the best coincidence in space and time were utilized. As we used both ascending and descending
250 MLS orbits, the acquisition time of MLS profiles varies between approximately either 14:00 or 01:30 in local solar time,
respectively, while the ground-based DIAL lidar profiles are only nocturnal (recorded at Reunion, i.e. approximately between
16:00 and 02:00 UTC). Even though the acquisition times do not overlap, we compared DIAL night profiles to daily MLS
profiles. However, because assimilated ozone profiles are retrieved regularly, time averaged assimilated profiles, from 18:00 to
00:00 UTC, were used for comparison with the corresponding DIAL profiles. As a result, the profile comparison is based on
255 the following formula:



$$\text{Relative}_{\text{bias}}(z) = 100 \times \frac{O_{3 \text{ DIAL}}(z) - O_{3 c}(z)}{O_{3 \text{ DIAL}}(z)}, \quad (1)$$

where $O_{3 \text{ DIAL}}(z)$ represents the stratospheric DIAL ozone value at altitude z and $O_{3 c}(z)$ represents the comparison ozone value (from MLS, MERRA-2 or M2-SCREAM) at the same altitude. Other statistical quantities were also determined, namely the number of profiles (N), the p-value, the coefficient of correlation (r), the linear regression (in the form $y = ax$) and the relative Root-Mean-Square Dispersion (RMSD) (see Appendix A). These statistical quantities were used to assess the differences and similarities between different ozone data in different layers.

3 Results

3.1 Aerosol plume

The HTHH main eruption occurred on 15 January and ejected large quantities of H_2O and SO_2 into the stratosphere (Khaykin et al., 2022; Sellitto et al., 2022; Zuo et al., 2022; Millán et al., 2022). Following the austral summer's general stratospheric circulation, the volcanic plume then traveled westward and reached the Indian Ocean and the African continent within days. The plume's transport across the Indian Ocean was captured by OMPS aerosol extinction profiles. Panels (b) to (e) of Fig. 1 present OMPS extinction profiles at 745 nm obtained over the Indian Ocean during the passage of the volcanic plume. Panel (a) presents a typical background aerosol distribution obtained prior to the plume's arrival over the Indian Ocean. At the bottom left of each panel are given the date and time of retrieval, and the black dots correspond to the instrument's estimation of the tropopause height. Panel (f) traces the satellite tracks corresponding to data in panels (a) to (e). Thus, this figure describes the latitudinal and vertical extension of the volcanic plume as seen from the satellite instrument's point of view during its passage over the Indian Ocean on 22 January. During unperturbed conditions (see Fig. 1a), aerosol distribution is vertically limited and confined within the troposphere, since largest values of the extinction coefficient are kept below the tropopause. However, the presence of the volcanic plume becomes clearly visible on the other panels, where large extinction coefficient values ($> 10^{-3}$) lie above the tropopause level. On 22 January (Fig. 1b to 1e), the volcanic plume is clearly visible in the stratosphere over the Indian Ocean between 5° S and 25° S , reaching altitudes greater than 35 km. Note that this result only characterizes the vertical and latitudinal extent of the volcanic plume, but it does not describe the longitudinal dimension of the plume. Equivalent observations can also be obtained for January 21 (not shown). Similar results were found by Taha et al. (2022) as they remarked the presence of a volcanic plume located at an altitude exceeding 36 km (Taha et al., 2022). Additionally, they reported that the high sensitivity of OMPS LP enabled to monitor the volcanic plume at altitudes above 36 km for a duration of up to 90 days.

Figure 2 shows the HTHH aerosol plume as seen by two quasi-colocalized instruments operating at the Maïdo observatory (lidar) and the Saint-Denis campus (sun-photometer). It is important to highlight that the two instruments are 20 km apart with an approximately 2000 m difference in elevation. Even though the AOD measured by the sun-photometer cannot be directly compared to the sAOD recorded by the lidar instrument, both sets of observations hold significant information about



the passage of the volcanic plume. Figure 2a depicts the evolution of the lidar aerosol extinction profiles at 532 nm between 21 and 23 January, and Fig. 2b shows the evolution of the lidar sAOD at 532 nm (in black) and sun-photometer level 2.0 total AOD (in red) at 532 nm for the second half of January 2022 with their respective uncertainties. The blue line represents the multi-year average of the sun-photometer level 2.0 data calculated from 2003 to 2021, and the shaded blue region is the corresponding $\pm 1\sigma$ (standard deviation). This multi-year average represents an average of AOD data which is grouped into months, irrespective of the years. Note that different horizontal axes are used for panels (a) and (b), and the shared temporal ranges are visually represented with gray regions. Note also that the Reunion sun-photometer did not record data at 532 nm. We instead converted data recorded at 675 nm to 532 nm using Angström exponent measurements between 440 and 675 nm.

Results show that the multi-year mean AOD of 0.05 ± 0.02 is very low in comparison to the maximum optical depth recorded by both instruments in January 2022. Indeed, after 20 January, total AOD values start to dramatically increase until 23 January, when they culminated at 0.57 ± 0.02 before gradually decreasing to return to background levels. Similarly to the sun-photometer measurements, the Maïdo lidar reveals an important amount of aerosols after 21 January, with sAOD values rising up to 0.84 ± 0.13 . A significant aerosol layer was seen by the lidar on two consecutive nights at altitudes of 29.7 km and 26.8 km, with maximum extinction coefficients of 0.53 ± 0.08 and 0.68 ± 0.06 , respectively. Note that sun-photometer measurements are obtained during the day, while lidar observations are only performed during nighttime. As such, observations from these two instruments cannot overlap as they do not operate simultaneously. A detailed study of the lidar observation of the HTHH plume can be found in Baron et al. (2023) (Baron et al., 2023).

3.2 Maïdo DIAL ozone profiles

Figure 3 shows the multi-year Maïdo DIAL ozone profiles. The black line depicts the altitude of the ozone maximum. A total of 470 profiles were obtained during the period from January 2013 to December 2021. The figure shows an ozone layer that is located between 22 and 27 km, and highlights the variation of the vertical distribution of ozone at Reunion. With a predominant annual cycle, the ozone maximum is at its highest altitude during austral summer (here in December at 26.3 km), and at its lowest altitude during austral winter (here in August at 23.7 km). This behavior, observed in subtropical (e.g., Reunion) and tropical locations, is attributed to changes in photochemistry and tropical upwelling as part of the Brewer-Dobson Circulation (BDC), which transports ozone from the equator (where it is primarily produced) to higher latitudes (Butchart, 2014; Plumb and Eluszkiewicz, 1999; Weber et al., 2011). During austral summer (winter), Reunion is closest to the ascending (descending) branch of the BDC, which explains why the ozone layer is highest (lowest) in altitude.

3.3 MLS, MERRA-2 and ERA5 ozone profiles

Prior to obtaining results relative to ozone measurements and stratospheric dynamics, we conducted a statistical analysis to determine the most accurate dataset for describing ozone levels in the study region during unperturbed condition. Thus, we compared MLS, MERRA-2 and ERA5 ozone concentration profiles obtained over Reunion to the Reunion stratospheric DIAL ozone concentration profiles from January 2013 to December 2021. Results are presented in Fig. 4 where the continuous line and the shaded area represent the mean relative bias and the standard error, respectively. This standard error represents standard



320 deviation divided by the square root of the number of individual comparisons (which varies as a function of altitude). The
aforementioned statistical quantities are also shown in the figure. These mean relative bias profiles were obtained by averaging
the results of Eq. (1) across all available ozone profiles. Similarly, the statistical results (correlation coefficient, linear regression
and relative RMSD) presented in the following were obtained from the comparison of all data points, irrespective of the altitude
level and date. Averaged mean relative bias and standard errors over several altitude ranges are summarized in Table 1.

325 Comparisons of MLS and MERRA-2 profiles to DIAL observations yield similar statistical quantities and similar mean
relative bias profiles. This similarity is expected as MERRA-2 incorporates MLS data into its assimilation process. Overall, the
best agreements are found in the 20–40 km altitude range, with higher and increasing deviations below 20 km and above 40
km (see Table 1). In the altitude range from 20 km to 40 km, MLS and MERRA-2 relative bias and error yield $-1.22 \pm 0.31 \%$
and $0.09 \pm 0.30 \%$, respectively. Above 40 km, MLS (MERRA-2) results show $3.73 \pm 2.22 \%$ ($11.87 \pm 1.94 \%$). Conversely,
330 below 20 km, one has $-0.06 \pm 1.95 \%$ ($4.28 \pm 1.81 \%$). On both mean relative bias profiles, there is a negative bias that appears
at ~ 20 km of altitude, with $-11.22 \pm 1.17 \%$ for MLS and $-12.69 \pm 0.67 \%$ for MERRA-2. Note that the increased difference
and error at altitudes greater than 40 km is partly due to the lidar signal-to-noise ratio decrease and to the reduced number of
lidar profiles reaching altitudes greater than 45 km. Indeed, out of the 470 lidar profiles, 410 reached 40 km, 132 reached 45
km and only 6 reached 47.5 km. Note also that the increased difference and error at altitudes lower than 20 km may be due to
335 the reduced satellite accuracy and precision (see Table 3.18.1 of (Livesey et al., 2022)) and the lower number of lidar profiles
for these altitudes. Indeed, out of the 470 profiles, 453 start below 20 km, 409 before 17.5 km and 131 before 15 km. For these
reasons, the MLS mean bias profile seems to under-estimate ozone concentrations by $20.73 \pm 1.60 \%$ at 16.70 km. ERA5, on
the other hand, shows accentuated differences with the DIAL profiles, with $-18.85 \pm 2.22 \%$ between 15 and 20 km, $0.79 \pm$
 0.31% between 20 and 40 km and $15.54 \pm 2.02 \%$ between 40 and 47.5 km. Note that the relative bias of ERA5 is greater
340 than that of MERRA-2, particularly in the troposphere and in the upper stratosphere.

Correlation coefficients ($r = 0.994$ for lidar–MLS and $r = 0.993$ for lidar–MERRA-2) indicate a very high correlation between
the lidar and both datasets, and linear regressions ($y = 1.013 x$ for lidar–MLS and $y = 1.024 x$ for lidar–MERRA-2) show that
satellite and assimilation profiles tend to slightly over-estimate ozone concentrations, irrespective of the altitude. Finally, a low
relative dispersion (RMSD = 7.542 % and RMSD = 8.130 % for MLS and MERRA-2, respectively) further demonstrates the
345 agreement between MLS or MERRA-2 and the DIAL profiles. While the correlation with ERA5 ($r = 0.992$) remains excellent,
the higher dispersion (RMSD = 9.216 %) and slope ($y = 1.039 x$) show the poorest agreement with the DIAL.

Therefore, the MLS and MERRA-2 ozone concentration profiles seem to be in good agreement with lidar observations in
the 20–40 km altitude range, which includes the altitudes of the HTHH volcanic plume (26–30 km) being our main focus in
this study.

350 3.4 Effects of the volcanic plume on ozone

Based on the good correlation and agreement between MERRA-2 and the stratospheric DIAL ozone profiles over Reunion, it
appears relevant to use MERRA-2 ozone products to investigate the changes in the distribution of the ozone anomaly over the
study region, giving the advantage of its highly resolved time and space coverage.



Figure 5 depicts ozone anomaly maps that show snapshots of the evolution of TCO and SCO reduction following the passage
355 of the volcanic plume over the Indian Ocean from 17 to 22 January. The ozone column anomalies (total and stratospheric) were
obtained by subtracting instantaneous ozone values from the averaged values calculated for the month of January over the pe-
riod from 2013 to 2021. The white dot symbols indicate the positions of local minima for both total and stratospheric ozone for
the given date and hour, whereas the stars indicate the positions of MERRA-2 total and stratospheric ozone minima throughout
the entire day. Additionally, the red dots on the figure indicate locations where MLS and MERRA-2 have nearly coincident
360 profiles near the HTHH aerosol plume. To ensure consistency across different measurements, only the MLS observations taken
during the ascending node were considered for these coincident observations. The profiles corresponding to these locations
were investigated and results are detailed at the end of this section. The anomaly maps emphasize that the study region was
subject to significant TCO and SCO anomalies over the latitudinal band from 30° S to 10° S, with a zonal westward transition
of the ozone minimum. These anomalies give rise to a structure resembling an ozone mini-hole extending over significant areas
365 of the studied region from 17 to 22 January. In fact, on 17 January, OMI recorded an ozone anomaly exceeding -15 DU over an
area of approximately 9.14×10^5 km². The TCO anomaly from MERRA-2 for the same day on panel (f) covered 12.06×10^5
km², and that for SCO from MERRA-2 on panel (k) extended over 9.57×10^5 km². The average ozone anomalies for these
regions are -36.33 DU for OMI, -27.78 DU for TCO from MERRA-2 and -26.38 DU for SCO from MERRA-2. Total and
stratospheric ozone columns (anomalies) over the minima (white dots) in panels (a), (f) and (k) are 160.7 DU (-98.76 DU,
370 or -38.06 %) for OMI, 208.49 DU (-48.66 DU, or -18.92 %) for total ozone from MERRA-2 and 183.86 DU (-42.7 DU, or
-18.85 %) for stratospheric ozone from MERRA-2. While the ozone anomaly appears to weaken during the transport process, it
continued to cover extensive regions of the Indian Ocean on 21 and 22 January. On January 22, the regions (average anomalies)
are 1.61×10^5 km² (-17.60 DU) for OMI on panel (e) and 4.94×10^5 km² (-18.08 DU) for TCO from MERRA-2 on panel (j).
SCO anomalies of up to -18.21 DU (-8.00 %) were still present in MERRA-2 data over the study region on 22 January, but
375 no anomaly exceeding -15 DU can be found on panel (o). MLS indicates a maximum SCO anomaly of -14.66 DU (-6.38 %)
within the ozone mini-hole structure on 20 January, and averaging MLS SCO anomalies from 18 to 22 January yields -5.43
DU (-2.26 %).

MERRA-2, M2-SCREAM and MLS ozone profiles retrieved from the locations marked by red dots are displayed in Fig.
6. The green lines represent multi-year profiles obtained from MLS. These multi-year profiles were obtained by averaging all
380 the profiles obtained in January over the study region from 2013 to 2021 and therefore represent a typical ozone profile for
background conditions. The shaded green area represents the $\pm 1\sigma$ (standard deviation) with respect to the mean value. As
Fig. 5 revealed local total and stratospheric ozone minima, Fig. 6 shows that these minima are due to reduction in the ozone
concentration in the ozone layer. Ozone profiles observed between 18 and 22 January exhibit a strong agreement among the
three datasets (MLS, MERRA-2, and M2-SCREAM). This is expected since both analyses are constrained by MLS. In the
385 altitude range from 20 to 30 km, MLS recorded a maximum anomaly of -17.57 DU (-12.27 %) on 20 January, compared to
the multi-year mean. The average of anomalies recorded by MLS between 18 to 22 January within this altitude range yields
-6.13 DU (-4.28 %). It should be noted that MERRA-2 indicates maximum ozone anomalies (not shown) of -26.58 DU (-18.42



%) within the same altitude range. However, there are clear differences between satellite and assimilation ozone results for 17 January which are discussed in Sect. 4.

390 Figure 7 displays TCO and SCO over the locations with the largest ozone reductions seen in MERRA-2 (stars in Fig. 5), for the whole month of January 2022. The dashed lines represent the multi-year average values derived from data collected between 2013 and 2021, and the shaded areas represent the $\pm 1\sigma$ (standard deviations). OMI TCO and MLS SCO were also obtained and are superimposed with red and green solid lines and dots, respectively. Similar to previous results, this figure clearly indicates that both TCO and SCO over central and western Australia were sensitive to the HTHH plume's overpass. 395 Indeed, the MERRA-2 SCO over central Australia (see Fig. 7a) plummeted to 183.71 DU on 17 January at 12:00 UTC, corresponding to an anomaly of -43.11 DU (-19.01 %) in comparison with the multi-year average value. As one may expect, this ozone reduction was also noticeable on the TCO (see Fig. 7a). OMI and MERRA-2 TCO fell to 204.98 DU and 208.73 DU, corresponding to anomalies of -52.32 DU (-20.33 %) and -48.56 DU (-18.87 %), respectively. Over western Australia (see Fig. 7b) on 18 January at 21:00 UTC, MERRA-2 SCO decreased to 197.34 DU, corresponding to an anomaly of -27.75 DU 400 (-14.06 %), and the MERRA-2 TCO fell to 233.06 DU, corresponding to an anomaly of -21.36 DU (-8.39 %). Similarly, OMI shows a sharp ozone decrease, but the values still lie within the multi-year average standard deviation. OMI TCO values for 18 January are 248.22 DU (-6.19 DU or -2.43 %). Similarly, the HTHH plume overpass appears to have had an impact on the MERRA-2 ozone columns over Madagascar (see Fig. 7c). SCO and TCO minima were found over Madagascar on 22 405 January at 03:00 UTC, with values of 209.26 DU and 229.74 DU, respectively, corresponding to anomalies of -18.21 DU (-8.00 %) and -25.05 DU (-9.83 %).

Even though the average values for January 2022 compare favorably between MLS and MERRA-2 observations for central Australia (232.40 DU and 229.77 DU, respectively), western Australia (233.10 DU and 229.68 DU, respectively) and Madagascar (236.18 and 234.61 DU, respectively), the amplitudes of the ozone minima are clearly different. The large stratospheric ozone minimum over Australia was not captured by MLS, whose minimum SCO recorded 227.73 DU on 18 January. MLS 410 indicates a clearer minimum of SCO over the point near Madagascar on 21 January, with levels decreasing to 221.12 DU. This observation differs from the values seen in MERRA-2 in the amplitude and date of this minimum value. Note that these differences are attributable to the fact that the locations studied here (stars in Fig. 5) do not directly correspond to MLS observation locations. Moreover, since the anomaly is moving, the all-day MERRA-2 minimum is likely to be different from the OMI or MLS value for that location.

415 3.5 Stratospheric dynamics

The Lagrangian HYSPLIT model was used to investigate the origin of the air-masses responsible for the ozone anomaly over the Indian Ocean following the HTHH eruption. Back-trajectories were run from the location of TCO minimum in the western region of the Indian Ocean, at the time at which this minimum was recorded, and for 9 distinct altitudes ranging between 22 and 26 km. Figure 8 shows the result of the HYSPLIT simulation, where the darkest trajectory represents air-masses at 26 km, 420 and the lightest trajectory represents air-masses at 22 km. Figure 8 shows that all back-trajectories are zonal, moving westward and passing over the location of the HTHH eruption. The results of the HYSPLIT back-trajectories simulation are consistent



with the lidar measurements made in Reunion (see Fig. 2), as well as with the ozone anomalies over the region of study as depicted in Fig. 5. Additionally, the latter shows a westward transition of ozone anomalies in the stratosphere over the Indian Ocean.

425 To support these results, we used ERA5 EPV contours to highlight the dynamics of the stratosphere at the 600 K potential temperature level (~ 24 km). Results for 18 January at 21:00 UTC and 22 January at 03:00 UTC are shown in Fig. 9, where EPV is expressed in potential vorticity units (PVU, with $1 \text{ PVU} = 10^{-6} \text{ m}^2 \text{ s}^{-1} \text{ K kg}^{-1}$). In this figure are also superimposed the SCO anomaly maps. The red line corresponds to the position of the subtropical barrier as estimated by DYBAL, and the white dot symbols indicate the location of SCO minima. When it enters the Indian Ocean on 18 January, the bulk of the stratospheric
430 ozone anomaly lies to the north of the subtropical barrier, itself located at an average global latitude of 26.6° S . In the course of its westward transport toward Madagascar, the bulk of the stratospheric anomaly stays north of the subtropical barrier (not shown). The region immediately north of the subtropical barrier, represented by the latitudinal band at $\sim 20^\circ \text{ S}$ between both stratospheric ozone minima, shows no discontinuity in PVU, thus allowing for isentropic transport from east to west on the 600 K isentropic surface. When the ozone anomaly exits the region of study on 22 January, the subtropical barrier (red thick
435 line in Fig. 9), located at an average global latitude of 24.8° S , is still distinctly south of the stratospheric ozone anomaly. Therefore, the east-to-west transport was made possible by the austral summer general stratospheric circulation, as well as the quasi-longitudinal EPV contours and the strong EPV gradient poleward.

4 Discussion

The HTHH eruption on 15 January 2022 injected enormous amounts of H_2O , aerosols, and a significant quantity of SO_2 into
440 the tropical stratosphere. As previously mentioned in Sect. 3, the presence of SO_2 within the volcanic plume had significant impacts on OMI observations, leading to biases in total ozone measurements. This is particularly the case on 17 January (see Fig. 5), but anomalies as severe as -42.13 DU (-16.40%) can still be found on 19 January and -29.32 DU (-11.11%) on 22 January. Employing a filtering method on 308 nm residuals within OMI TCO level 2 data removes most, if not all, of the volcanic induced errors (not shown). Applying this filter on 17 January data eliminates almost entirely the ozone anomaly. The
445 application of this filter in the following days continued to remove parts of the anomaly until 22 January. Therefore, level 3 OMI TCO data may certainly be affected by errors induced by the volcanic aerosol plume. Additionally, because it incorporates OMI data into its assimilation process, MERRA-2 ozone fields are also expected to be influenced by OMI measurements. Since MLS did not record any anomalies on 17 January, the initial anomaly observed by MERRA-2 on that day is primarily derived from anomalous OMI data. Therefore, the ozone anomalies described in the previous section with MERRA-2 and
450 OMI results might not have been as severe as depicted here, but their spatial localization should be accurate. Furthermore, because MERRA-2 lacked concurrent MLS profiles, the vertical structure of this anomaly was not accurately represented. Consequently, the algorithm distributed the TCO increment vertically based on the background error estimate (Wargan et al., 2017). In MERRA-2, these background error standard deviations are linked to the background ozone mixing ratio, leading to the majority of the anomaly being placed around the ozone maximum in the stratosphere. However, as subsequent days



455 unfolded, the vertical placement of the anomaly gradually evolved and became more realistic, owing to the gradual acquisition
of MLS observations, which provided additional insights into its structure. This could explain why MLS and MERRA-2 data
do not converge prior to 18 January in Fig. 6.

The cause of the ozone anomaly can stem from multiple causes and may result from a combination of various factors.
First, the low ozone levels reported in this article are likely influenced by the injection of tropospheric ozone-poor air into the
460 stratosphere. Considering the short chemical lifetime of ozone at the altitudes where we observed ozone anomalies (~22–28
km or 40–15 hPa), it is expected that ozone levels would have rebounded from this initial impact before reaching the western
part of the Indian Ocean. However, as pointed out by Legras et al. (2022), the concomitant injection of SO₂ and H₂O might
have contributed to a fast increase of the stratospheric aerosol burden after the eruption by increasing the amount of sulfate
aerosols which are known to deplete ozone (Legras et al., 2022). Furthermore, as underlined by Tie and Brasseur (1995),
465 the decline in ozone levels following a major volcanic eruption is linked to the combined presence of SO₂ and chlorine (Tie
and Brasseur, 1995). Justifiably, Zhu et al. (2023) suggested that ozone losses within the volcanic plume resulted from the
enhanced HO_x and ClO_x cycles enabled by the simultaneous injection of H₂O, ClO and HCl (Zhu et al., 2023). Therefore,
the ozone reduction seen in Sect. 3 is likely the outcome of multiple factors, including the injection of ozone-poor air-masses,
the presence and production of sulfate aerosols, and the influence of the HO_x and ClO_x cycles.

470 Due to the low vertical resolution of satellite and assimilation profiles (about 1.1 km resolution for MERRA-2), and due to
the lower sampling frequency by MLS, results regarding the amount and altitude of ozone anomaly should be interpreted with
caution. The diminution of the altitude at which ozone anomaly occurs in Fig. 6, shifting from 25–28 km on 18 January to
22–28 km on 22 January, might be due to the satellite sampling different parts of the plume on different days. Nonetheless, a
sedimentation process of the aerosol plume has been documented by Legras et al. (2022). According to their study, following
475 the initial rapid removal of ice and ash, the remaining volcanic plume formed two distinct cloud layers, located between 26
and 32 km in altitude, traveling westward (Legras et al., 2022; Baron et al., 2023). The rapid descent of the aerosol plume
in the first week after the eruption might also explain in part the descent of the ozone anomaly, but this remains to be more
investigated.

5 Conclusions

480 The Hunga Tonga-Hunga Ha'apai (HTHH) volcano's main eruption occurred on 15 January 2022, releasing massive amounts
of aerosols, sulfur dioxide and water vapor into the atmosphere (Sellitto et al., 2022; Zuo et al., 2022; Millán et al., 2022).
The volcanic plume was observed to have vertically extended through the troposphere and stratosphere, and it was also shown
that some ejected material even reached the mesosphere (Carr et al., 2022). OMPS aerosol extinction profiles revealed that this
volcanic plume did indeed extend through the entire troposphere and above, stretched between 5° S and 25° S and reached
485 altitudes greater than 35 km over the Indian Ocean. These results are supported by the Maïdo aerosol lidar, which observed
the plume during two consecutive nights a few days after the eruption, indicating that the core of the plume was passing over
Reunion at an altitude ranging from 26.8 to 29.7 km.



The dynamics of the stratosphere responsible for the volcanic plume's advection over the Indian Ocean were studied using ERA5 EPV maps. The HYSPLIT simulation highlighted the presence of the summer's westward stratospheric flow. ERA5 EPV maps indicated that the region situated between Australia and Reunion showed no PVU discontinuity at the 600 K isentropic level during the passage of the volcanic plume. Thus, due to isentropic transport and the summer's westward stratospheric flow, the volcanic plume traveled westward and reached the Indian Ocean and Reunion within days, confirming the results of previous studies.

The ozone anomaly associated with the volcanic plume was investigated using OMI, MLS, MERRA-2 and M2-SCREAM ozone data, taking advantage of the fine temporal and spatial resolution of assimilation datasets. However, it must be noted that early ozone results from OMI, MERRA-2 and M2-SCREAM are expected to be significantly influenced by the presence of the volcanic aerosol plume and SO₂.

Still, being able to localize the anomaly and observe its displacement, we hypothesize that the advection of the volcanic aerosol plume had an impact on ozone levels over the Indian Ocean, as an ozone mini-hole structure was found to extend over large areas of the studied region from 17 January to 22 January. Specifically, the TCO anomaly of -15 DU from MERRA-2 covers an area of 12.06×10^5 km² on 17 January and 4.94×10^5 km² on 22 January. Total and stratospheric ozone columns reached a minimum over Australia's central regions, although this early ozone loss may be attributable to the injection of ozone-poor tropospheric air-masses and the interference of observations with SO₂. The ozone anomaly then followed the displacement of the volcanic aerosol plume in an east-to-west motion. MLS profiles indicate a maximum SCO anomaly of (-14.66 DU or -6.38%) within the ozone mini-hole structure on 20 January. Average MLS SCO anomalies from 18 to 22 January yield -5.43 DU (-2.26 %). As subsequent days unfolded and as more MLS profiles became available, assimilation results became more realistic. A closer examination of the MLS, MERRA-2 and M2-SCREAM ozone profiles revealed that the ozone decrease occurs at altitudes ranging from 20 to 30 km, which corresponds to the location of the tropical ozone layer. Within this altitude range, MLS recorded a maximum anomaly on 20 January, with -17.57 DU (-12.27 %). An average of the anomalies recorded by MLS within this altitude range yields -6.13 DU (-4.28 %).

This study showed the evolution of the localization of the early ozone anomaly in the HTHH volcanic aerosol plume in the Indian Ocean. We examined the impact of this aerosol plume on ozone levels, yet interference in the measurements prevents us from obtaining precise and reliable ozone anomalies for this event. This would require the use of meso-scale models that incorporate a comprehensive representation of stratospheric chemistry and dynamics, as well as the perturbations caused by the HTHH.

Appendix A: Statistical parameters

Statistical parameters were used to for comparisons between lidar and satellite or assimilation data. Here we chose to use the correlation coefficient (r) and the Root-Mean-Square Dispersion (RMSD) to assess the differences and agreements between datasets in different layers of the atmosphere. They are based on the following equations:



$$520 \quad r = \frac{\sum_{i=1}^N (O_{3 \text{ DIAL}_i} - \overline{O_{3 \text{ DIAL}}}) \times (O_{3 \text{ c}_i} - \overline{O_{3 \text{ c}}})}{\sqrt{\sum_{i=1}^N (O_{3 \text{ DIAL}_i} - \overline{O_{3 \text{ DIAL}}})^2} \times \sqrt{\sum_{i=1}^N (O_{3 \text{ c}_i} - \overline{O_{3 \text{ c}}})^2}}, \quad (\text{A1})$$

$$\text{RMSD} = \sqrt{\frac{1}{N} \sum_{i=1}^N (O_{3 \text{ DIAL}_i} - O_{3 \text{ c}_i})^2}, \quad (\text{A2})$$

where N is the number of available profiles, $O_{3 \text{ c}_i}$ represents the ozone data compared to DIAL ($O_{3 \text{ DIAL}_i}$) observations, and the index i iterates over the available profiles at different time steps. For each coincident profile, individual values of r and RMSD are obtained. The r and RMSD values reported in Sect. 3 are the averages derived from the individual r and RMSD values across all compared profiles.

Data availability. Reunion aerosol lidar and used in this steady are accessible from <https://doi.org/10.5281/zenodo.7790283> (last accessed on 14 September 2023). Reunion ozone lidar measurements are available through the NDACC page (<https://ndacc.larc.nasa.gov/>, last accessed on 23 August 2023). OMI, MLS and MERRA-2 data can be downloaded using NASA's data portal (<https://disc.gsfc.nasa.gov/>, last accessed on 23 August 2023). M2-SCREAM data can be accessed using this specific link: <https://disc.gsfc.nasa.gov/datasets?keywords=M2-SCREAM&page=1> (last accessed on 23 August 2023). ERA5 reanalyses can be obtained from ECMWF's Climate Data Store (<https://cds.climate.copernicus.eu#!/home>, last accessed on 23 August 2023). AERONET Version 3 Level 2 data are available through this link: <https://aeronet.gsfc.nasa.gov/> (last accessed on 23 August 2023). OMPS data can be accessed from <https://ozoneaq.gsfc.nasa.gov/> (last accessed on 23 August 2023). HYSPLIT back-trajectories can be obtained from https://www.ready.noaa.gov/HYSPLIT_traj.php (last accessed on 23 August 2023).

Author contributions. TM was the project leader; HB was the supervisor of the project; HB and NB participated in the methodology interpretation of the results; all co-authors participated in the review of the manuscript.

Competing interests. The authors declare that they have no conflict of interest.

Acknowledgements. The authors acknowledge the French South-African PROTEA program and the CNRS-NRF IRP ARSAIO (Atmospheric Research in Southern Africa and Indian Ocean) project for supporting research activities, as well as the Conseil Régional de la Réunion for the Ph.D. scholarship of Tristan Millet. The authors thank NASA for facilitating easy access and providing documentation for OMPS, MLS, OMI, MERRA-2 and M2-SCREAM data. The authors extend their thank to ECMWF for providing access to ERA5 data and the NOAA-ARL for supplying the HYSPLIT transport and dispersion model. The authors are appreciative of the PIs for providing data and their respective



545 teams for maintaining the lidars and AERONET stations used in the present article. The authors from LACy acknowledge the support of the European Commission through the REALISTIC project (GA 101086690). Lucien Froidevaux is warmly thanked for providing insights into MLS ozone data. Finally, the first author expresses heartfelt gratitude to Krzysztof Wargan for his significant contribution in aiding the understanding of MERRA-2 results and for providing valuable remarks that have improved the quality of the article.



References

- Andreae, M. O. and Merlet, P.: Emission of trace gases and aerosols from biomass burning, *Global Biogeochemical Cycles*, 15, 955–966, <https://doi.org/https://doi.org/10.1029/2000GB001382>, 2001.
- 550 Baldy, S., Ancellet, G., Bessafi, M., Badr, A., and Luk, D. L. S.: Field observations of the vertical distribution of tropospheric ozone at the island of Reunion (southern tropics), *Journal of Geophysical Research: Atmospheres*, 101, 23 835–23 849, <https://doi.org/https://doi.org/10.1029/95JD02929>, 1996.
- Baray, J. L., Courcoux, Y., Keckhut, P., Portafaix, T., Tulet, P., Cammas, J. P., Hauchecorne, A., Godin Beekmann, S., De Mazière, M., Hermans, C., Desmet, F., Sellegri, K., Colomb, A., Ramonet, M., Sciare, J., Vuillemin, C., Hoareau, C., Dionisi, D., Duflot, V., Vérémes, H., Porteneuve, J., Gabarrot, F., Gaudo, T., Metzger, J. M., Payen, G., Leclair de Bellevue, J., Barthe, C., Posny, F., Ricaud, P., Abchiche, A., and Delmas, R.: Maïdo observatory: a new high-altitude station facility at Reunion Island (21° S, 55° E) for long-term atmospheric remote sensing and in situ measurements, *Atmospheric Measurement Techniques*, 6, 2865–2877, <https://doi.org/10.5194/amt-6-2865-2013>, 2013.
- 555
- Baron, A., Chazette, P., Khaykin, S., Payen, G., Marquestaut, N., Bègue, N., and Duflot, V.: Early Evolution of the Stratospheric Aerosol Plume Following the 2022 Hunga Tonga-Hunga Ha’apai Eruption: Lidar Observations From Reunion (21°S, 55°E), *Geophysical Research Letters*, 50, e2022GL101 751, <https://doi.org/https://doi.org/10.1029/2022GL101751>, e2022GL101751 2022GL101751, 2023.
- 560
- Bègue, N., Bencherif, H., Sivakumar, V., Kirgis, G., Mze, N., and Leclair de Bellevue, J.: Temperature variability and trends in the UT-LS over a subtropical site: Reunion (20.8° S, 55.5° E), *Atmospheric Chemistry & Physics*, 10, 8563–8574, <https://doi.org/10.5194/acp-10-8563-2010>, 2010.
- 565
- Bencherif, H., Portafaix, T., Baray, J. L., Morel, B., Baldy, S., Leveau, J., Hauchecorne, A., Keckhut, P., Moorgawa, A., Michaelis, M. M., and Diab, R.: LIDAR observations of lower stratospheric aerosols over South Africa linked to large scale transport across the southern subtropical barrier, *Journal of Atmospheric and Solar-Terrestrial Physics*, 65, 707–715, [https://doi.org/10.1016/S1364-6826\(03\)00006-3](https://doi.org/10.1016/S1364-6826(03)00006-3), 2003.
- Bencherif, H., Amraoui, L. E., Semane, N., Massart, S., Charyulu, D. V., Hauchecorne, A., and Peuch, V. H.: Examination of the 2002 major warming in the southern hemisphere using ground-based and Odin/SMR assimilated data: stratospheric ozone distributions and tropic/mid-latitude exchange, *Canadian Journal of Physics*, 85, 1287–1300, <https://doi.org/10.1139/P07-143>, 2007.
- 570
- Bencherif, H., El Amraoui, L., Kirgis, G., Leclair de Bellevue, J., Hauchecorne, A., Mzé, N., Portafaix, T., Pazmino, A., and Goutail, F.: Analysis of a rapid increase of stratospheric ozone during late austral summer 2008 over Kerguelen (49.4° S, 70.3° E), *Atmospheric Chemistry & Physics*, 11, 363–373, <https://doi.org/10.5194/acp-11-363-2011>, 2011.
- 575
- Bencherif, H., Bègue, N., Kirsch Pinheiro, D., du Preez, D. J., Cadet, J.-M., da Silva Lopes, F. J., Shikwambana, L., Landolfo, E., Vescovini, T., Labuschagne, C., Silva, J. J., Anabor, V., Coheur, P.-F., Mbatha, N., Hadji-Lazaro, J., Sivakumar, V., and Clerbaux, C.: Investigating the Long-Range Transport of Aerosol Plumes Following the Amazon Fires (August 2019): A Multi-Instrumental Approach from Ground-Based and Satellite Observations, *Remote Sensing*, 12, 3846, <https://doi.org/10.3390/rs12223846>, 2020.
- Bernhard, G. H., Neale, R. E., Barnes, P. W., Neale, P. J., Zepp, R. G., Wilson, S. R., Andrady, A. L., Bais, A. F., McKenzie, R. L., Aucamp, P. J., Young, P. J., Liley, J. B., Lucas, R. M., Yazar, S., Rhodes, L. E., Byrne, S. N., Hollestein, L. M., Olsen, C. M., Young, A. R., Robson, T. M., Bornman, J. F., Jansen, M. A. K., Robinson, S. A., Ballaré, C. L., Williamson, C. E., Rose, K. C., Banaszak, A. T., Häder, D.-P., Hylander, S., Wängberg, S.-Å., Austin, A. T., Hou, W.-C., Paul, N. D., Madronich, S., Sulzberger, B., Solomon, K. R., Li, H., Schikowski, T., Longstreth, J., Pandey, K. K., Heikkilä, A. M., and White, C. C.: Environmental effects of stratospheric ozone depletion, UV radiation
- 580



- and interactions with climate change: UNEP Environmental Effects Assessment Panel, update 2019, *Photochem. Photobiol. Sci.*, 19, 542–584, <https://doi.org/10.1039/D0PP90011G>, 2020.
- 585 Butchart, N.: The Brewer-Dobson circulation, *Reviews of Geophysics*, 52, 157–184, <https://doi.org/https://doi.org/10.1002/2013RG000448>, 2014.
- Carr, J. L., Horváth, A., Wu, D. L., and Friberg, M. D.: Stereo Plume Height and Motion Retrievals for the Record-Setting Hunga Tonga-Hunga Ha’apai Eruption of 15 January 2022, *Geophysical Research Letters*, 49, e2022GL098131, <https://doi.org/https://doi.org/10.1029/2022GL098131>, e2022GL098131 2022GL098131, 2022.
- 590 Clain, G., Baray, J.-L., Delmas, R., Keckhut, P., and Cammas, J.-P.: A lagrangian approach to analyse the tropospheric ozone climatology in the tropics: Climatology of stratosphere–troposphere exchange at Reunion Island, *Atmospheric Environment*, 44, 968–975, <https://doi.org/https://doi.org/10.1016/j.atmosenv.2009.08.048>, 2010.
- Coy, L., Newman, P. A., Wargan, K., Partyka, G., Strahan, S. E., and Pawson, S.: Stratospheric Circulation Changes Associated With the Hunga Tonga-Hunga Ha’apai Eruption, *Geophysical Research Letters*, 49, e2022GL100982, <https://doi.org/https://doi.org/10.1029/2022GL100982>, e2022GL100982 2022GL100982, 2022.
- 595 Dhomse, S. S., Kinnison, D., Chipperfield, M. P., Salawitch, R. J., Cionni, I., Hegglin, M. I., Abraham, N. L., Akiyoshi, H., Archibald, A. T., Bednarz, E. M., Bekki, S., Braesicke, P., Butchart, N., Dameris, M., Deushi, M., Frith, S., Hardiman, S. C., Hassler, B., Horowitz, L. W., Hu, R.-M., Jöckel, P., Josse, B., Kirner, O., Kremser, S., Langematz, U., Lewis, J., Marchand, M., Lin, M., Mancini, E., Marécal, V., Michou, M., Morgenstern, O., O’Connor, F. M., Oman, L., Pitari, G., Plummer, D. A., Pyle, J. A., Revell, L. E., Rozanov, E., Schofield, R., Stenke, A., Stone, K., Sudo, K., Tilmes, S., Vioni, D., Yamashita, Y., and Zeng, G.: Estimates of ozone return dates from Chemistry-Climate Model Initiative simulations, *Atmospheric Chemistry and Physics*, 18, 8409–8438, <https://doi.org/10.5194/acp-18-8409-2018>, 2018.
- 600 Draxler, R. and Hess, G.: Description of the HYSPLIT_4 modelling system, NOAA Tech. Mem. ERL ARL-224, 1997.
- 605 Draxler, R. and Hess, G.: An overview of the HYSPLIT_4 modelling system for trajectories, dispersion, and deposition, *Australian Meteorological Magazine*, 47, 295–308, 1998.
- Duflot, V., Dils, B., Baray, J. L., De Mazière, M., Attié, J. L., Vanhaelewyn, G., Senten, C., Vigouroux, C., Clain, G., and Delmas, R.: Analysis of the origin of the distribution of CO in the subtropical southern Indian Ocean in 2007, *Journal of Geophysical Research: Atmospheres*, 115, <https://doi.org/https://doi.org/10.1029/2010JD013994>, 2010.
- 610 Duflot, V., Royer, P., Chazette, P., Baray, J. L., Courcoux, Y., and Delmas, R.: Marine and biomass burning aerosols in the southern Indian Ocean: Retrieval of aerosol optical properties from shipborne lidar and Sun photometer measurements, *Journal of Geophysical Research (Atmospheres)*, 116, D18208, <https://doi.org/10.1029/2011JD015839>, 2011.
- Gelaro, R., McCarty, W., Suárez, M. J., Todling, R., Molod, A., Takacs, L., Randles, C. A., Darmenov, A., Bosilovich, M. G., Reichle, R., Wargan, K., Coy, L., Cullather, R., Draper, C., Akella, S., Buchard, V., Conaty, A., da Silva, A. M., Gu, W., Kim, G.-K., Koster, R., Lucchesi, R., Merkova, D., Nielsen, J. E., Partyka, G., Pawson, S., Putman, W., Rienecker, M., Schubert, S. D., Sienkiewicz, M., and Zhao, B.: The Modern-Era Retrospective Analysis for Research and Applications, Version 2 (MERRA-2), *Journal of Climate*, 30, 5419–5454, <https://doi.org/10.1175/JCLI-D-16-0758.1>, 2017.
- 615 Giles, D. M., Sinyuk, A., Sorokin, M. G., Schafer, J. S., Smirnov, A., Slutsker, I., Eck, T. F., Holben, B. N., Lewis, J. R., Campbell, J. R., Welton, E. J., Korkin, S. V., and Lyapustin, A. I.: Advancements in the Aerosol Robotic Network (AERONET) Version 3 database – automated near-real-time quality control algorithm with improved cloud screening for Sun photometer aerosol optical depth (AOD) measurements, *Atmospheric Measurement Techniques*, 12, 169–209, <https://doi.org/10.5194/amt-12-169-2019>, 2019.
- 620



- Global Modeling and Assimilation Office (GMAO): MERRA-2 inst3_3d_asm_Nv: 3d, 3-Hourly, Instantaneous, Model-Level, Assimilation, Assimilated Meteorological Fields V5.12.4, Greenbelt, MD, USA, Goddard Earth Sciences Data and Information Services Center (GES DISC). Accessed: [September 2022], <https://doi.org/10.5067/WWQSQ8IVFW8>, 2015a.
- 625 Global Modeling and Assimilation Office (GMAO): MERRA-2 inst1_2d_asm_Nx: 2d, 1-Hourly, Instantaneous, Single-Level, Assimilation, Single-Level Diagnostics V5.12.4, Greenbelt, MD, USA, Goddard Earth Sciences Data and Information Services Center (GES DISC). Accessed: [September 2022], <https://doi.org/10.5067/3Z173KIE2TPD>, 2015b.
- Gobbi, G. P., Congeduti, F., and Adriani, A.: Early stratospheric effects of the Pinatubo Eruption, *Geophysical Research Letters*, 19, 997–1000, <https://doi.org/https://doi.org/10.1029/92GL01038>, 1992.
- 630 Godin-Beekmann, S., Porteneuve, J., and Garnier, A.: Systematic DIAL lidar monitoring of the stratospheric ozone vertical distribution at Observatoire de Haute-Provence (43.92 N, 5.71 E), *Journal of environmental Monitoring*, 5, 57–67, 2003.
- Guo, S., Bluth, G. J. S., Rose, W. I., Watson, I. M., and Prata, A. J.: Re-evaluation of SO₂ release of the 15 June 1991 Pinatubo eruption using ultraviolet and infrared satellite sensors, *Geochemistry, Geophysics, Geosystems*, 5, <https://doi.org/https://doi.org/10.1029/2003GC000654>, 2004.
- 635 Hofmann, D. J. and Oltmans, S. J.: Anomalous Antarctic ozone during 1992: Evidence for Pinatubo volcanic aerosol effects, *Journal of Geophysical Research: Atmospheres*, 98, 18 555–18 561, <https://doi.org/https://doi.org/10.1029/93JD02092>, 1993.
- Hofmann, D. J. and Solomon, S.: Ozone destruction through heterogeneous chemistry following the eruption of El Chichón, *Journal of Geophysical Research: Atmospheres*, 94, 5029–5041, <https://doi.org/https://doi.org/10.1029/JD094iD04p05029>, 1989.
- Holton, J. R., Haynes, P. H., McIntyre, M. E., Douglass, A. R., Rood, R. B., and Pfister, L.: Stratosphere-troposphere exchange, *Reviews of Geophysics*, 33, 403–439, <https://doi.org/https://doi.org/10.1029/95RG02097>, 1995.
- 640 Hoskins, B. J., McIntyre, M. E., and Robertson, A. W.: On the use and significance of isentropic potential vorticity maps, *Quarterly Journal of the Royal Meteorological Society*, 111, 877–946, <https://doi.org/10.1002/qj.49711147002>, 1985.
- IPCC: Climate Change 2013: The Physical Science Basis. Contribution of Working Group I to the Fifth Assessment Report of the Intergovernmental Panel on Climate Change, in: Cambridge University Press, <https://www.ipcc.ch/report/ar5/wg1/>, 2013.
- 645 IPCC: Climate Change 2021: The Physical Science Basis. Contribution of Working Group I to the Sixth Assessment Report of the Intergovernmental Panel on Climate Change, in: Cambridge University Press, <https://www.ipcc.ch/report/ar6/wg1/>, 2021.
- Ivatt, P. D., Evans, M. J., and Lewis, A. C.: Suppression of surface ozone by an aerosol-inhibited photochemical ozone regime, *Nature Geoscience*, 15, 536–540, <https://doi.org/10.1038/s41561-022-00972-9>, 2022.
- Ivy, D. J., Solomon, S., Kinnison, D., Mills, M. J., Schmidt, A., and Neely III, R. R.: The influence of the Calbuco eruption
650 on the 2015 Antarctic ozone hole in a fully coupled chemistry-climate model, *Geophysical Research Letters*, 44, 2556–2561, <https://doi.org/https://doi.org/10.1002/2016GL071925>, 2017.
- Jacob, D. J.: Introduction to atmospheric chemistry, Princeton University Press, 1999.
- Jaffe, D. A. and Wigder, N. L.: Ozone production from wildfires: A critical review, *Atmospheric Environment*, 51, 1–10, <https://doi.org/https://doi.org/10.1016/j.atmosenv.2011.11.063>, 2012.
- 655 Jenkins, S., Smith, C., Allen, M., and Grainger, R.: Tonga eruption increases chance of temporary surface temperature anomaly above 1.5°C, *Nature Climate Change*, 13, 127–129, <https://doi.org/10.1038/s41558-022-01568-2>, 2023.
- Khaykin, S., Podglajen, A., Ploeger, F., Grooß, J.-U., Tence, F., Bekki, S., Khlopenkov, K., Bedka, K., Rieger, L., Baron, A., Godin-Beekmann, S., Legras, B., Sellitto, P., Sakai, T., Barnes, J., Uchino, O., Morino, I., Nagai, T., Wing, R., Baumgarten, G., Gerding, M., Dufлот, V., Payen, G., Jumelet, J., Querel, R., Liley, B., Bourassa, A., Clouser, B., Feofilov, A., Hauchecorne, A., and Ravetta,



- 660 F.: Global perturbation of stratospheric water and aerosol burden by Hunga eruption, *Communications Earth & Environment*, 3, 316, <https://doi.org/10.1038/s43247-022-00652-x>, 2022.
- Kirchner, I., Stenchikov, G. L., Graf, H.-F., Robock, A., and Antuña, J. C.: Climate model simulation of winter warming and summer cooling following the 1991 Mount Pinatubo volcanic eruption, *Journal of Geophysical Research: Atmospheres*, 104, 19 039–19 055, <https://doi.org/https://doi.org/10.1029/1999JD900213>, 1999.
- 665 Koster, R. D., McCarty, W., Coy, L., Gelaro, R., Huang, A., Merkova, D., Smith, E. B., Sienkiewicz, M., and Wargan, K.: MERRA-2 input observations: Summary and assessment, Tech. rep., 2016.
- Legras, B., Duchamp, C., Sellitto, P., Podglajen, A., Carboni, E., Siddans, R., Grooß, J.-U., Khaykin, S., and Ploeger, F.: The evolution and dynamics of the Hunga Tonga–Hunga Ha’apai sulfate aerosol plume in the stratosphere, *Atmospheric Chemistry and Physics*, 22, 14 957–14 970, <https://doi.org/10.5194/acp-22-14957-2022>, 2022.
- 670 Levelt, P., van den Oord, G., Dobber, M., Malkki, A., Visser, H., de Vries, J., Stammes, P., Lundell, J., and Saari, H.: The ozone monitoring instrument, *IEEE Transactions on Geoscience and Remote Sensing*, 44, 1093–1101, <https://doi.org/10.1109/TGRS.2006.872333>, 2006.
- Levelt, P. F., Joiner, J., Tamminen, J., Veefkind, J. P., Bhartia, P. K., Stein Zweers, D. C., Duncan, B. N., Streets, D. G., Eskes, H., van der A, R., McLinden, C., Fioletov, V., Carn, S., de Laat, J., DeLand, M., Marchenko, S., McPeters, R., Ziemke, J., Fu, D., Liu, X., Pickering, K., Apituley, A., González Abad, G., Arola, A., Boersma, F., Chan Miller, C., Chance, K., de Graaf, M., Hakkarainen, J., Hassinen, S.,
- 675 Ialongo, I., Kleipool, Q., Krotkov, N., Li, C., Lamsal, L., Newman, P., Nowlan, C., Suleiman, R., Tilstra, L. G., Torres, O., Wang, H., and Wargan, K.: The Ozone Monitoring Instrument: overview of 14 years in space, *Atmospheric Chemistry and Physics*, 18, 5699–5745, <https://doi.org/10.5194/acp-18-5699-2018>, 2018.
- Livesey, N., Froidevaux, L., Santee, M., Read, W., Lambert, A., Wu, D., Jiang, J., Manney, G., Schwartz, M., and Su, H.: An overview of Aura Microwave Limb Sounder measurements and key results in the upper troposphere and lower stratosphere, in: 37th COSPAR
- 680 Scientific Assembly, vol. 37, p. 1810, 2008.
- Livesey, N. J., Read, W. G., Wagner, P. A., Froidevaux, L., Santee, M. L., Schwartz, M. J., Lambert, A., Valle, L. F. M., Pumphrey, H. C., Manney, G. L., Fuller, R. A., Jarnot, R. F., Knosp, B. W., and Lay, R. R.: Version 5.0x Level 2 and 3 data quality and description document., https://mls.jpl.nasa.gov/data/v5-0_data_quality_document.pdf, 2022.
- Manney, G. L., Millán, L. F., Santee, M. L., Wargan, K., Lambert, A., Neu, J. L., Werner, F., Lawrence, Z. D., Schwartz, M. J., Livesey, N. J., and Read, W. G.: Signatures of Anomalous Transport in the 2019/2020 Arctic Stratospheric Polar Vortex, *Journal of Geophysical Research: Atmospheres*, 127, e2022JD037 407, <https://doi.org/https://doi.org/10.1029/2022JD037407>, e2022JD037407 2022JD037407, 2022.
- Manney, G. L., Santee, M. L., Lambert, A., Millán, L. F., Minschwaner, K., Werner, F., Lawrence, Z. D., Read, W. G., Livesey, N. J., and Wang, T.: Siege in the Southern Stratosphere: Hunga Tonga–Hunga Ha’apai Water Vapor Excluded From the 2022 Antarctic Polar Vortex, *Geophysical Research Letters*, 50, e2023GL103 855, <https://doi.org/https://doi.org/10.1029/2023GL103855>, e2023GL103855 2023GL103855, 2023.
- 690 Matsumura, Y. and Ananthaswamy, H. N.: Toxic effects of ultraviolet radiation on the skin, *Toxicology and Applied Pharmacology*, 195, 298–308, <https://doi.org/https://doi.org/10.1016/j.taap.2003.08.019>, toxicology of the Skin, 2004.
- McCormick, M., Thomason, L., and Trepte, C.: Atmospheric effects of the Mt Pinatubo eruption, *Nature*, 373, 399–404, <https://www.nature.com/articles/373399a0>, 1995.
- 695



- Mills, G., Sharps, K., Simpson, D., Pleijel, H., Frei, M., Burkey, K., Emberson, L., Uddling, J., Broberg, M., Feng, Z., Kobayashi, K., and Agrawal, M.: Closing the global ozone yield gap: Quantification and cobenefits for multistress tolerance, *Global Change Biology*, 24, 4869–4893, <https://doi.org/https://doi.org/10.1111/gcb.14381>, 2018.
- 700 Millán, L., Santee, M. L., Lambert, A., Livesey, N. J., Werner, F., Schwartz, M. J., Pumphrey, H. C., Manney, G. L., Wang, Y., Su, H., Wu, L., Read, W. G., and Froidevaux, L.: The Hunga Tonga-Hunga Ha’apai Hydration of the Stratosphere, *Geophysical Research Letters*, 49, e2022GL099381, <https://doi.org/https://doi.org/10.1029/2022GL099381>, e2022GL099381 2022GL099381, 2022.
- Morel, B., Bencherif, H., Keckhut, P., Portafaix, T., Hauchecorne, A., and Baldy, S.: Fine-scale study of a thick stratospheric ozone lamina at the edge of the southern subtropical barrier: 2. Numerical simulations with coupled dynamics models, *Journal of Geophysical Research (Atmospheres)*, 110, D17101, <https://doi.org/10.1029/2004JD005737>, 2005.
- 705 Nakamura, N.: Two-Dimensional Mixing, Edge Formation, and Permeability Diagnosed in an Area Coordinate, *Journal of Atmospheric Sciences*, 53, 1524 – 1537, [https://doi.org/10.1175/1520-0469\(1996\)053<1524:TDMEFA>2.0.CO;2](https://doi.org/10.1175/1520-0469(1996)053<1524:TDMEFA>2.0.CO;2), 1996.
- National Oceanic and Atmospheric Administration (NOAA): Global Data Assimilation System (GDAS), <https://www.ready.noaa.gov/data/archives/gdas1/>, accessed September 2022, 2023.
- Nielsen, J. E., Pawson, S., Molod, A., Auer, B., da Silva, A. M., Douglass, A. R., Duncan, B., Liang, Q., Manyin, M., Oman, L. D., Putman, 710 W., Strahan, S. E., and Wargan, K.: Chemical Mechanisms and Their Applications in the Goddard Earth Observing System (GEOS) Earth System Model, *Journal of Advances in Modeling Earth Systems*, 9, 3019–3044, <https://doi.org/https://doi.org/10.1002/2017MS001011>, 2017.
- Nuvolone, D., Petri, D., and Voller, F.: The Effects of Ozone on Human Health, *Environmental Science and Pollution Research*, 25, 8074–8088, <https://doi.org/10.1007/s11356-017-9239-3>, 2018.
- 715 OMI team: Ozone Monitoring Instrument (OMI) data user’s guide, Tech. rep., [https://www.shuomingshuku.com/download/OZONE-MONITORING-INSTRUMENT-\(OMI\)-DATA-USER-GUIDE.PDF](https://www.shuomingshuku.com/download/OZONE-MONITORING-INSTRUMENT-(OMI)-DATA-USER-GUIDE.PDF), 2012.
- Organization, W. M.: Scientific assessment of ozone depletion: 1998, Global ozone research and monitoring project-report no. 44, WMO, <https://library.wmo.int/idurl/4/50254>, 1999.
- Organization, W. M.: Scientific assessment of ozone depletion: 2018, Global ozone research and monitoring project-report no. 58, WMO, 720 <https://library.wmo.int/idurl/4/56362>, 2018.
- Pazmiño, A.: DIAL lidar for ozone measurements, in: *Journal de Physique IV (Proceedings)*, vol. 139, pp. 361–372, EDP sciences, 2006.
- Pitts, D. G., Cullen, A. P., and Hacker, P. D.: Ocular effects of ultraviolet radiation from 295 to 365 nm., *Investigative Ophthalmology & Visual Science*, 16, 932–939, 1977.
- Plumb, R. A. and Eluszkiewicz, J.: The Brewer–Dobson Circulation: Dynamics of the Tropical Upwelling, *Journal of the Atmospheric 725 Sciences*, 56, 868 – 890, [https://doi.org/https://doi.org/10.1175/1520-0469\(1999\)056<0868:TBDCDO>2.0.CO;2](https://doi.org/https://doi.org/10.1175/1520-0469(1999)056<0868:TBDCDO>2.0.CO;2), 1999.
- Portafaix, T., Morel, B., Bencherif, H., Baldy, S., Godin-Beekmann, S., and Hauchecorne, A.: Fine-scale study of a thick stratospheric ozone lamina at the edge of the southern subtropical barrier, *Journal of Geophysical Research (Atmospheres)*, 108, 4196, <https://doi.org/10.1029/2002JD002741>, 2003.
- Portafaix, T., Godin-Beekmann, S., Payen, G., Langerock, B., Fernandez, S., Posny, F., Cammas, J.-P., Metzger, J.-M., Bencherif, H., 730 Vigouroux, C., and Marquestaut, N.: Ozone profiles obtained by DIAL technique at Maïdo Observatory in La Réunion Island: comparisons with ECC ozone-sondes, ground-based FTIR spectrometer and microwave radiometer measurements, *EPJ Web of Conferences*, 119, <https://doi.org/10.1051/epjconf/201611905005>, 2015.



- Ramaswamy, V., Schwarzkopf, M. D., Randel, W. J., Santer, B. D., Soden, B. J., and Stenchikov, G. L.: Anthropogenic and Natural Influences in the Evolution of Lower Stratospheric Cooling, *Science*, 311, 1138–1141, <https://doi.org/10.1126/science.1122587>, 2006.
- 735 Ranaivombola, M., Bègue, N., Bencherif, H., Millet, T., Sivakumar, V., Dufлот, V., Baron, A., Mbatha, N., Piketh, S., Formenti, P., et al.: Aerosol Optical Properties and Types over Southern Africa and Reunion Island Determined from Ground-Based and Satellite Observations over a 13-Year Period (2008–2021), *Remote Sensing*, 15, 1581, 2023.
- Randriambelo, T., Baray, J.-L., and Baldy, S.: Effect of biomass burning, convective venting, and transport on tropospheric ozone over the Indian Ocean: Reunion Island field observations, *Journal of Geophysical Research: Atmospheres*, 105, 11 813–11 832, <https://doi.org/https://doi.org/10.1029/1999JD901097>, 2000.
- 740 Robock, A.: Volcanic eruptions and climate, *Reviews of Geophysics*, 38, 191–219, <https://doi.org/https://doi.org/10.1029/1998RG000054>, 2000.
- Rowland, F. S.: Stratospheric ozone depletion by chlorofluorocarbons (Nobel lecture), *Angewandte Chemie International Edition in English*, 35, 1786–1798, 1996.
- 745 Sellitto, P., Podglajen, A., Belhadji, R., Boichu, M., Carboni, E., Cuesta, J., Duchamp, C., Kloss, C., Siddans, R., Bègue, N., Blarel, L., Jegou, F., Khaykin, S., Renard, J.-B., and Legras, B.: The unexpected radiative impact of the Hunga Tonga eruption of 15th January 2022, *Communications Earth & Environment*, 3, 288, <https://doi.org/10.1038/s43247-022-00618-z>, 2022.
- Semane, N., Bencherif, H., Morel, B., Hauchecorne, A., and Diab, R. D.: An unusual stratospheric ozone decrease in the Southern Hemisphere subtropics linked to isentropic air-mass transport as observed over Irene (25.5° S, 28.1° E) in mid-May 2002, *Atmospheric Chemistry & Physics*, 6, 1927–1936, <https://doi.org/10.5194/acp-6-1927-2006>, 2006.
- 750 Sivakumar, V., Bencherif, H., Bègue, N., and Thompson, A. M.: Tropopause Characteristics and Variability from 11 yr of SHADOZ Observations in the Southern Tropics and Subtropics, *Journal of Applied Meteorology and Climatology*, 50, 1403–1416, <https://doi.org/10.1175/2011JAMC2453.1>, 2011.
- Solomon, S.: Stratospheric ozone depletion: A review of concepts and history, *Reviews of Geophysics*, 37, 275–316, <https://doi.org/https://doi.org/10.1029/1999RG900008>, 1999.
- 755 Stenchikov, G. L., Kirchner, I., Robock, A., Graf, H.-F., Antuña, J. C., Grainger, R. G., Lambert, A., and Thomason, L.: Radiative forcing from the 1991 Mount Pinatubo volcanic eruption, *Journal of Geophysical Research: Atmospheres*, 103, 13 837–13 857, <https://doi.org/https://doi.org/10.1029/98JD00693>, 1998.
- Taha, G., Loughman, R., Zhu, T., Thomason, L., Kar, J., Rieger, L., and Bourassa, A.: OMPS LP Version 2.0 multi-wavelength aerosol extinction coefficient retrieval algorithm, *Atmospheric Measurement Techniques*, 14, 1015–1036, <https://doi.org/10.5194/amt-14-1015-2021>, 2021.
- 760 Taha, G., Loughman, R., Colarco, P. R., Zhu, T., Thomason, L. W., and Jaross, G.: Tracking the 2022 Hunga Tonga-Hunga Ha’apai Aerosol Cloud in the Upper and Middle Stratosphere Using Space-Based Observations, *Geophysical Research Letters*, 49, e2022GL100091, <https://doi.org/https://doi.org/10.1029/2022GL100091>, e2022GL100091 2022GL100091, 2022.
- 765 Tie, X. and Brasseur, G.: The response of stratospheric ozone to volcanic eruptions: Sensitivity to atmospheric chlorine loading, *Geophysical Research Letters*, 22, 3035–3038, <https://doi.org/https://doi.org/10.1029/95GL03057>, 1995.
- Tohir, A. M., Portafaix, T., Sivakumar, V., Bencherif, H., Pazmiño, A., and Bègue, N.: Variability and trend in ozone over the southern tropics and subtropics, *Annales Geophysicae*, 36, 381–404, <https://doi.org/10.5194/angeo-36-381-2018>, 2018.
- Vigouroux, C., Stavrou, T., Whaley, C., Dils, B., Dufлот, V., Hermans, C., Kumps, N., Metzger, J.-M., Scolas, F., Vanhaelewyn, G., Müller, J.-F., Jones, D. B. A., Li, Q., and De Mazière, M.: FTIR time-series of biomass burning products (HCN, C₂H₆, C₂H₂, CH₃OH, and
- 770



- HCOOH) at Reunion Island (21° S, 55° E) and comparisons with model data, *Atmospheric Chemistry and Physics*, 12, 10367–10385, <https://doi.org/10.5194/acp-12-10367-2012>, 2012.
- 775 Wang, X., Randel, W., Zhu, Y., Tilmes, S., Starr, J., Yu, W., Garcia, R., Toon, B., Park, M., Kinnison, D., Bourassa, A., Rieger, L., and Li, J.: Stratospheric climate anomalies and ozone loss caused by the Hunga Tonga volcanic eruption, <https://doi.org/10.1002/essoar.10512922.1>, 2022.
- Wargan, K., Labow, G., Frith, S., Pawson, S., Livesey, N., and Partyka, G.: Evaluation of the Ozone Fields in NASA's MERRA-2 Reanalysis, *Journal of Climate*, 30, 2961 – 2988, <https://doi.org/10.1175/JCLI-D-16-0699.1>, 2017.
- Wargan, K., Weir, B., Manney, G. L., Cohn, S. E., Knowland, K. E., Wales, P. A., and Livesey, N. J.: M2-SCREAM: A stratospheric composition reanalysis of Aura MLS data with MERRA-2 transport, *Earth and Space Science*, 10, e2022EA002632, 2023.
- 780 Waters, J., Froidevaux, L., Harwood, R., Jarnot, R., Pickett, H., Read, W., Siegel, P., Cofield, R., Filipiak, M., Flower, D., Holden, J., Lau, G., Livesey, N., Manney, G., Pumphrey, H., Santee, M., Wu, D., Cuddy, D., Lay, R., Loo, M., Perun, V., Schwartz, M., Stek, P., Thurstans, R., Boyles, M., Chandra, K., Chavez, M., Chen, G.-S., Chudasama, B., Dodge, R., Fuller, R., Girard, M., Jiang, J., Jiang, Y., Knosp, B., LaBelle, R., Lam, J., Lee, K., Miller, D., Oswald, J., Patel, N., Pukala, D., Quintero, O., Scaff, D., Van Snyder, W., Tope, M., Wagner, P., and Walch, M.: The Earth observing system microwave limb sounder (EOS MLS) on the aura Satellite, *IEEE Transactions on Geoscience and Remote Sensing*, 44, 1075–1092, <https://doi.org/10.1109/TGRS.2006.873771>, 2006.
- 785 Weber, M., Dikty, S., Burrows, J. P., Garny, H., Dameris, M., Kubin, A., Abalichin, J., and Langematz, U.: The Brewer-Dobson circulation and total ozone from seasonal to decadal time scales, *Atmospheric Chemistry and Physics*, 11, 11221–11235, <https://doi.org/10.5194/acp-11-11221-2011>, 2011.
- Yook, S., Thompson, D. W. J., and Solomon, S.: Climate Impacts and Potential Drivers of the Unprecedented Antarctic Ozone Holes of 2020 and 2021, *Geophysical Research Letters*, 49, e2022GL098064, <https://doi.org/https://doi.org/10.1029/2022GL098064>, e2022GL098064 2022GL098064, 2022.
- 790 Zhu, Y., Toon, O. B., Kinnison, D., Harvey, V. L., Mills, M. J., Bardeen, C. G., Pitts, M., Bègue, N., Renard, J.-B., Berthet, G., and Jégou, F.: Stratospheric Aerosols, Polar Stratospheric Clouds, and Polar Ozone Depletion After the Mount Calbuco Eruption in 2015, *Journal of Geophysical Research: Atmospheres*, 123, 12,308–12,331, <https://doi.org/https://doi.org/10.1029/2018JD028974>, 2018.
- 795 Zhu, Y., Portmann, R. W., Kinnison, D., Toon, O. B., Millán, L., Zhang, J., Vömel, H., Tilmes, S., Bardeen, C. G., Wang, X., Evan, S., Randel, W. J., and Rosenlof, K. H.: Stratospheric ozone depletion inside the volcanic plume shortly after the 2022 Hunga Tonga eruption, *EGUsphere*, 2023, 1–18, <https://doi.org/10.5194/egusphere-2023-1334>, 2023.
- Zuo, M., Zhou, T., Man, W., Chen, X., Liu, J., Liu, F., and Gao, C.: Volcanoes and Climate: Sizing up the Impact of the Recent Hunga Tonga-Hunga Ha'apai Volcanic Eruption from a Historical Perspective, *Advances in Atmospheric Sciences*, <https://doi.org/10.1007/s00376-022-2034-1>, 2022.
- 800

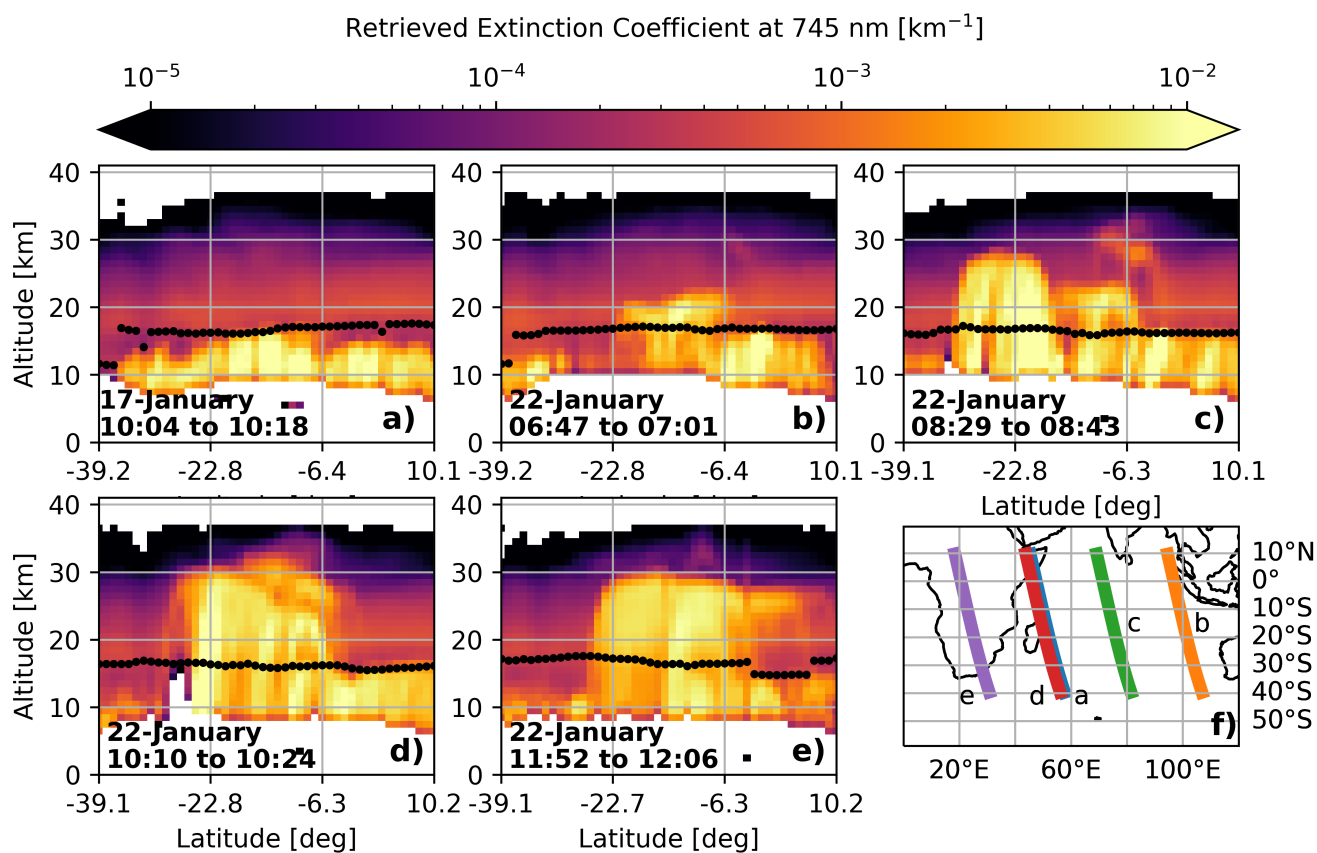


Figure 1. OMPS-LP aerosol extinction height-latitude cross-sections over the Indian Ocean at 745 nm for **a)** background conditions prior to the passage of the volcanic plume on 17 January and **b–e)** during the passage of the plume on 22 January. Panel **f)** shows the satellite track corresponding to each overpass. The superimposed black dots on panels **a–e)** indicate the instrument's estimation of the tropopause height.

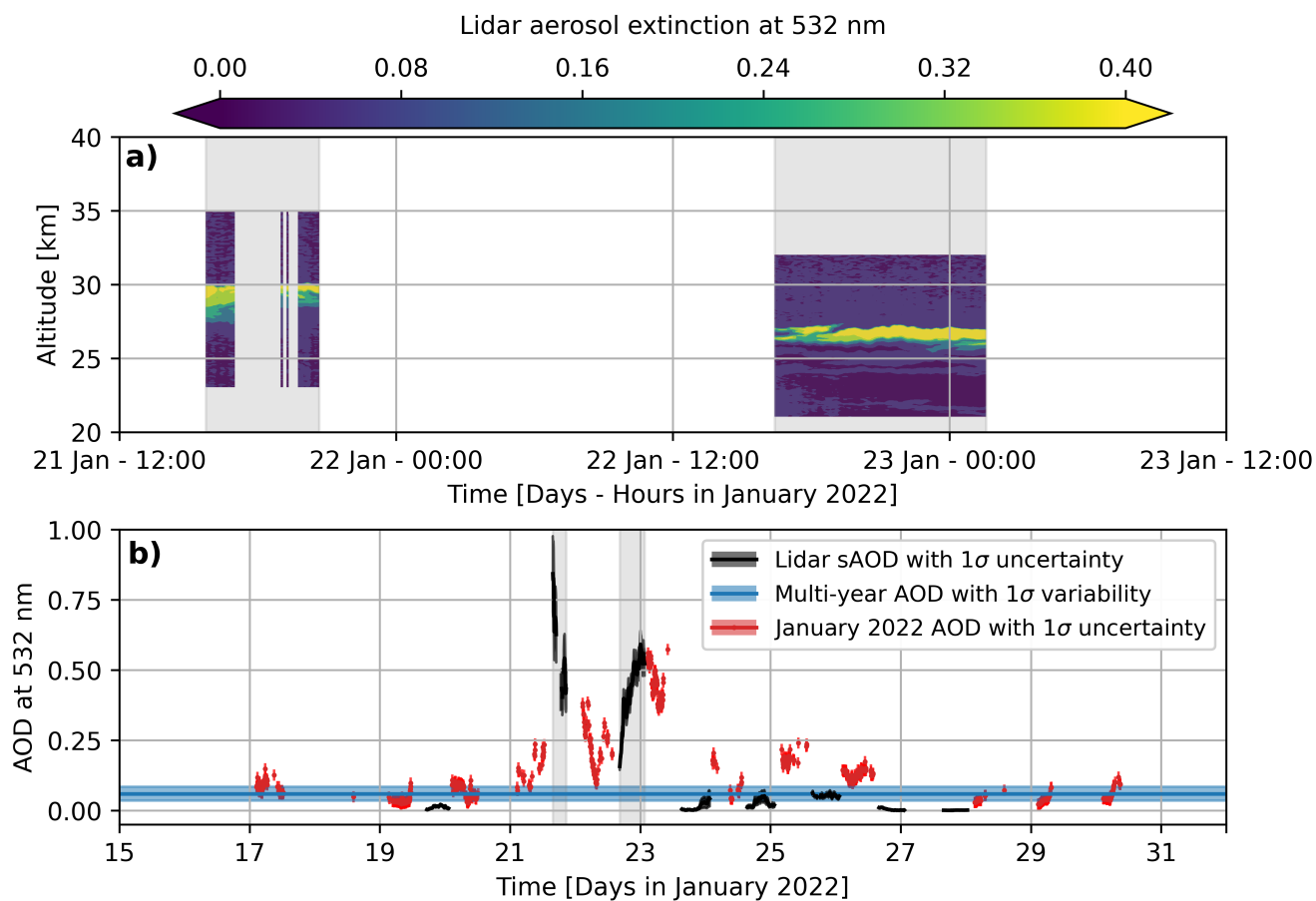


Figure 2. Aerosol lidar extinction profiles at 532 nm (a) and aerosol lidar stratospheric AOD (sAOD) in black with level 2.0 sun-photometer total AOD in red and their associated uncertainties (b). The blue line and shaded area represent average and standard deviation values given by level 2.0 sun-photometer data from 2003 to 2021. The shared temporal ranges in both panels are visually represented with gray regions.

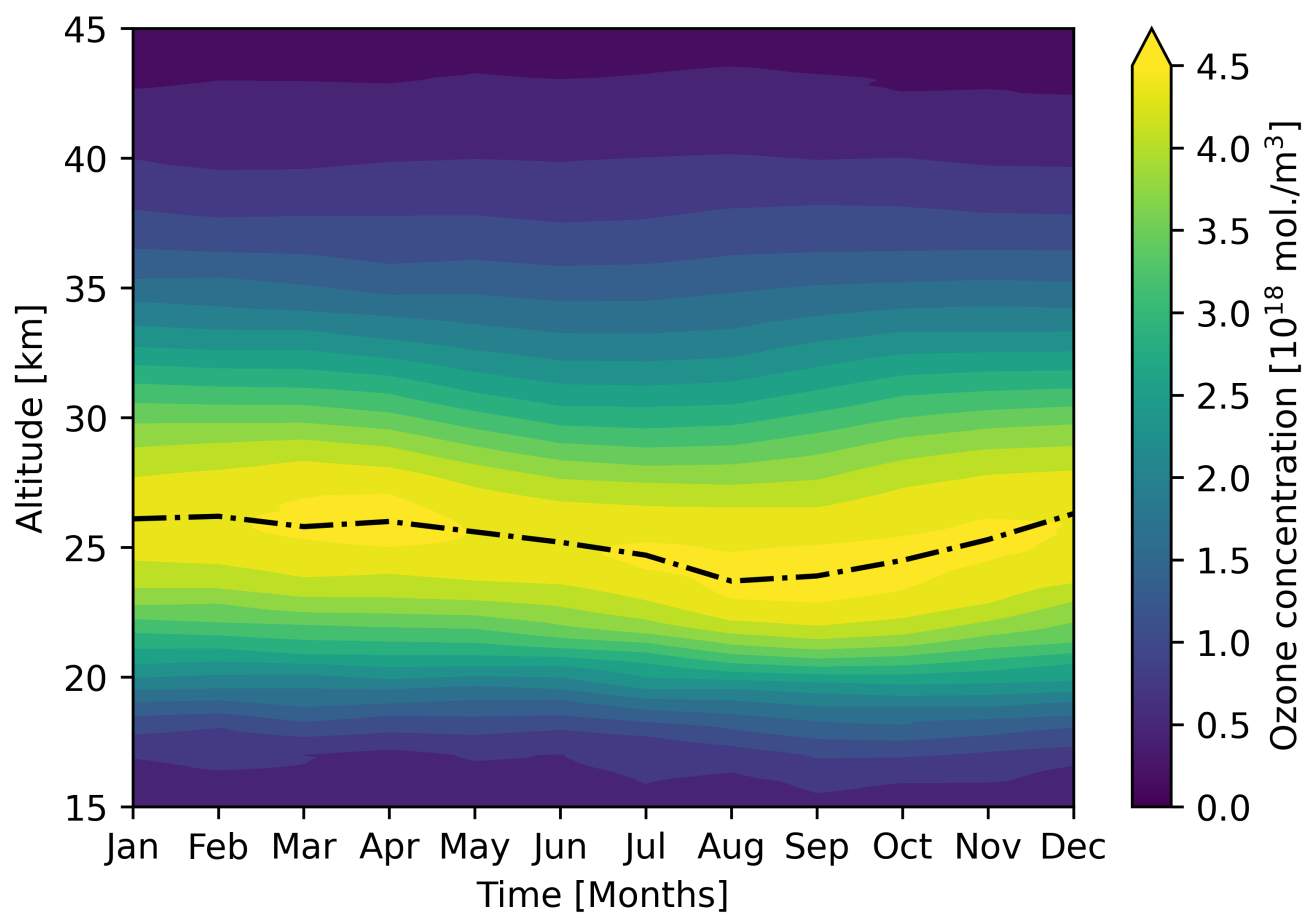


Figure 3. Multi-year stratospheric DIAL profiles obtained from observations between 2013 and 2021 at Reunion. The black dotted line shows the altitude of the ozone maximum.

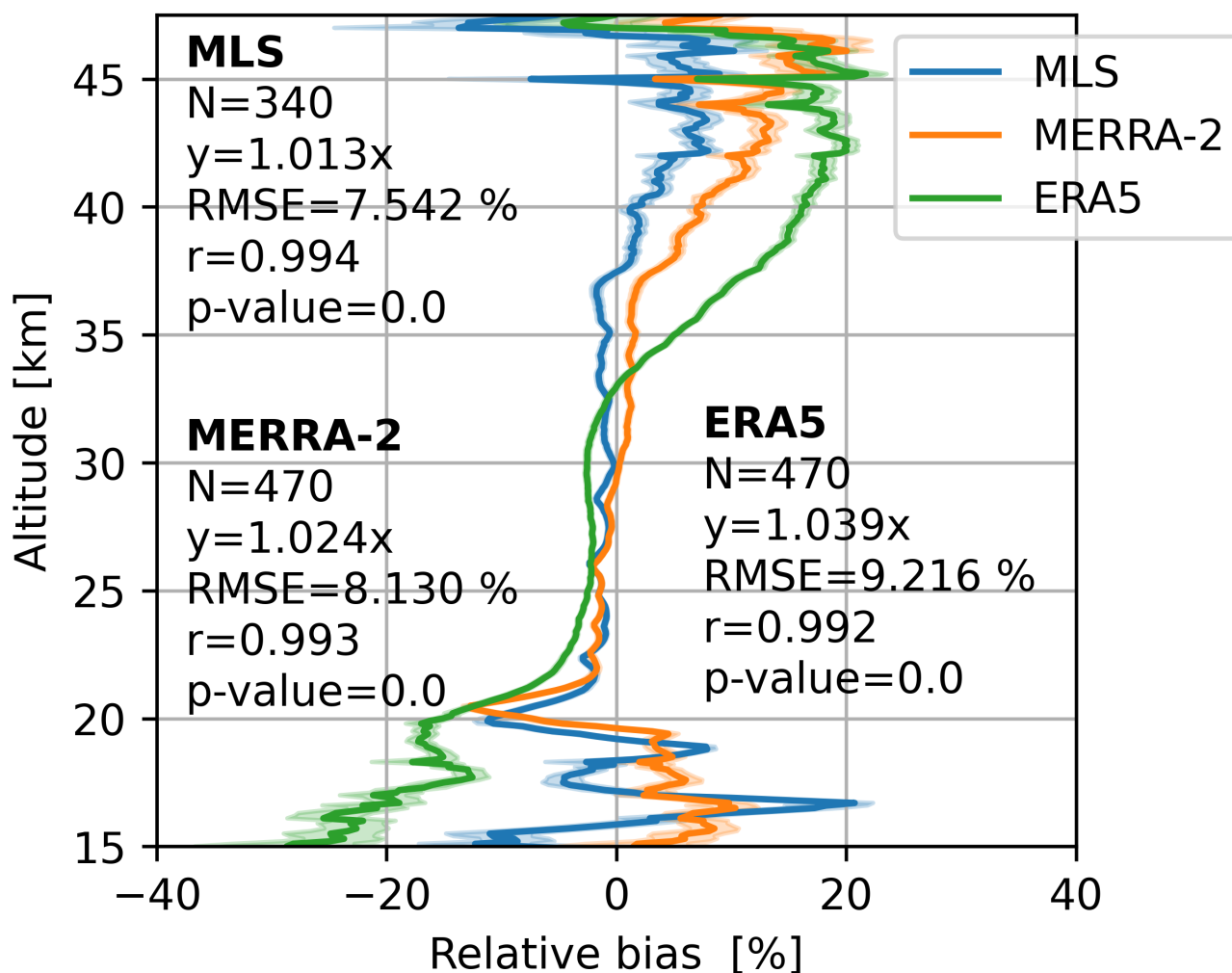


Figure 4. Mean relative bias (solid line) and $\pm 1\sigma$ standard error (shaded area) comparing nocturnal DIAL ozone profiles to the corresponding MLS, MERRA-2 and ERA5 ozone profiles between January 2013 and December 2021.



Table 1. Averaged mean relative bias and standard error for the comparisons between MLS, MERRA-2, ERA5 and the DIAL observations over the 15–20 km, 20–40 km and 40–47.5 km altitude ranges.

	15–20 km	20–40 km	40–47.5 km
Lidar/MLS	-0.06% ± 1.95%	-1.22% ± 0.31%	3.73% ± 2.22%
Lidar/MERRA-2	4.28% ± 1.81%	0.09% ± 0.30%	11.87% ± 1.94%
Lidar/ERA5	-18.85% ± 2.22%	0.79% ± 0.31%	15.54% ± 2.02%

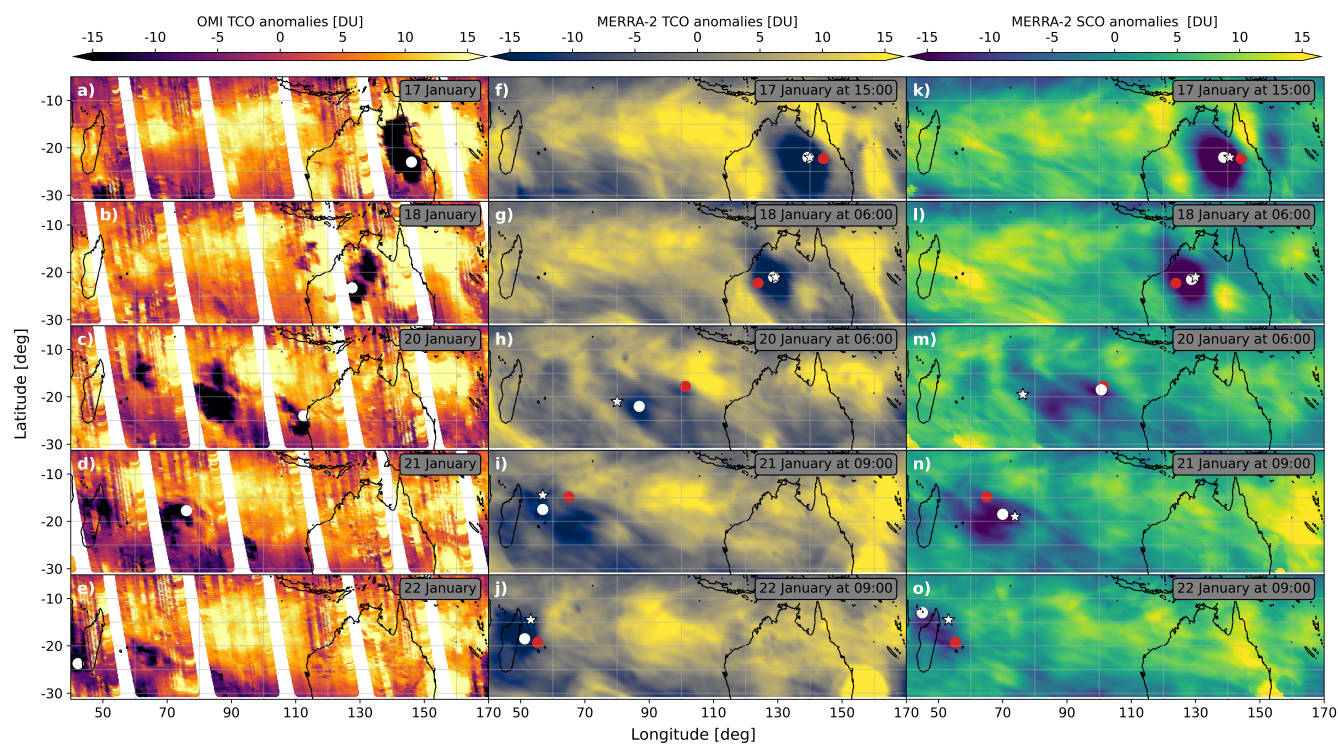


Figure 5. Time evolution of total ozone anomalies from OMI (left column) and MERRA-2 (middle column), together with stratospheric ozone anomalies from MERRA-2 (right column), from 17 to 22 January 2022. The red dots represent the locations of MLS profiles, each matched to the nearest MERRA-2 grid point, the white dots represent the locations of ozone minima for the given date and hour shown, and the stars represent the locations of total and stratospheric ozone minima from MERRA-2 throughout the entire day. Date and time of acquisition are shown in the top right corner of each panel.

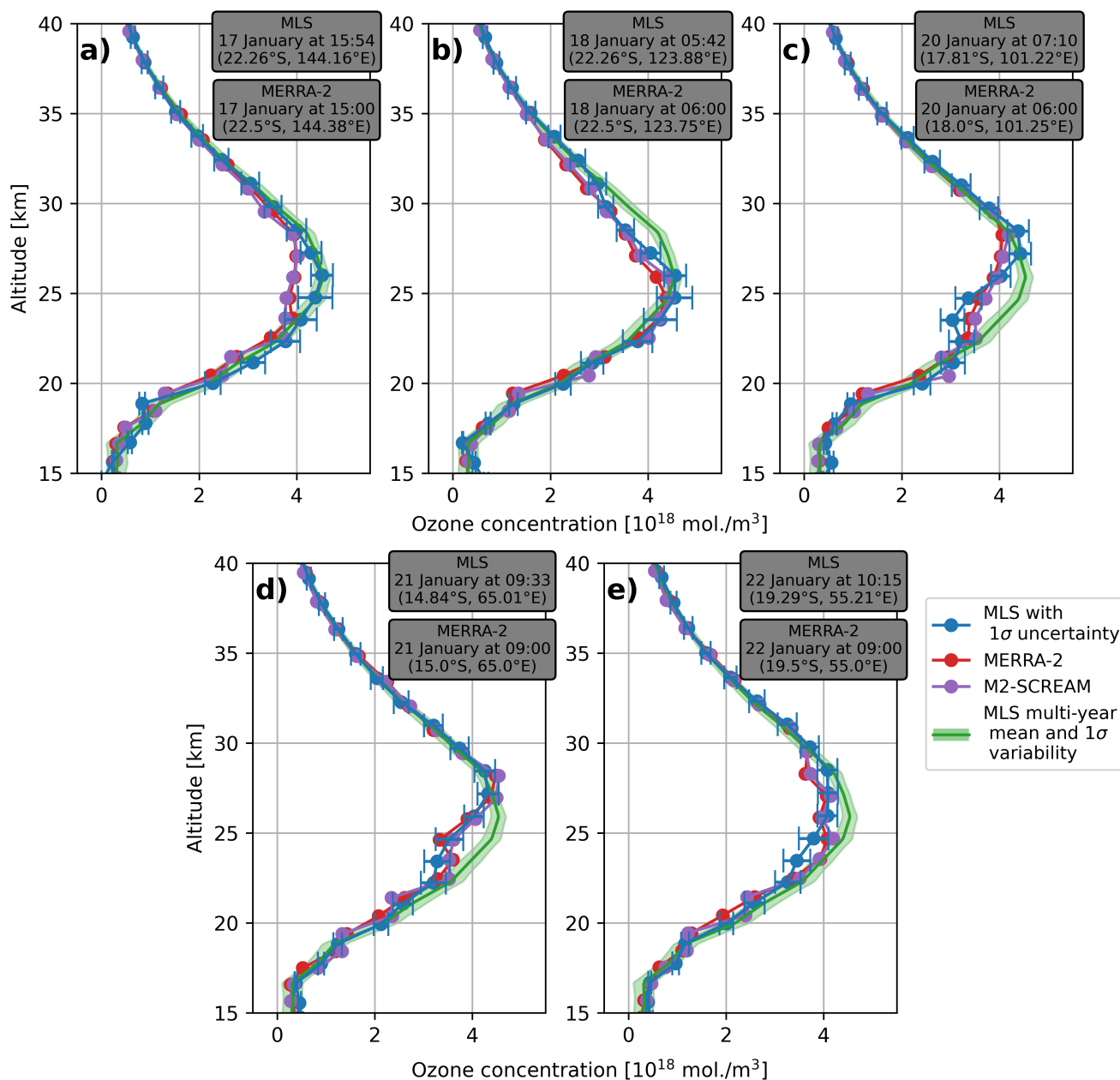


Figure 6. MLS, MERRA-2 and M2-SCREAM ozone profiles for the locations marked by red dots in Fig. 5. The green curves (shaded areas) depict the January average MLS profiles ($\pm 1\sigma$ standard deviation) over the 2013–2021 period for the whole study region. Locations and times of retrieval are displayed on the top right corner of each panel.

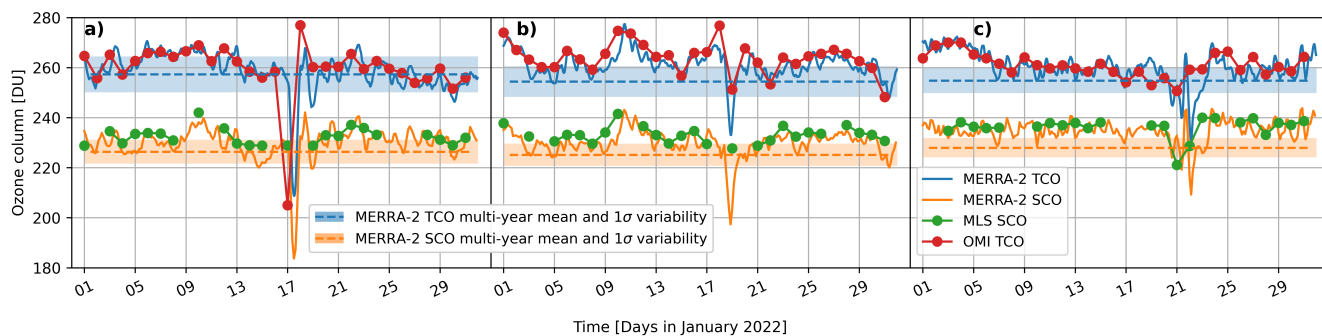


Figure 7. Time evolution of MERRA-2 and OMI TCO as well as MERRA-2 and MLS SCO over the locations with minimal ozone levels represented by stars in Fig. 5. Results concerning central regions of Australia, western regions of Australia and northern regions of Madagascar appear in panels a), b) and c), respectively.

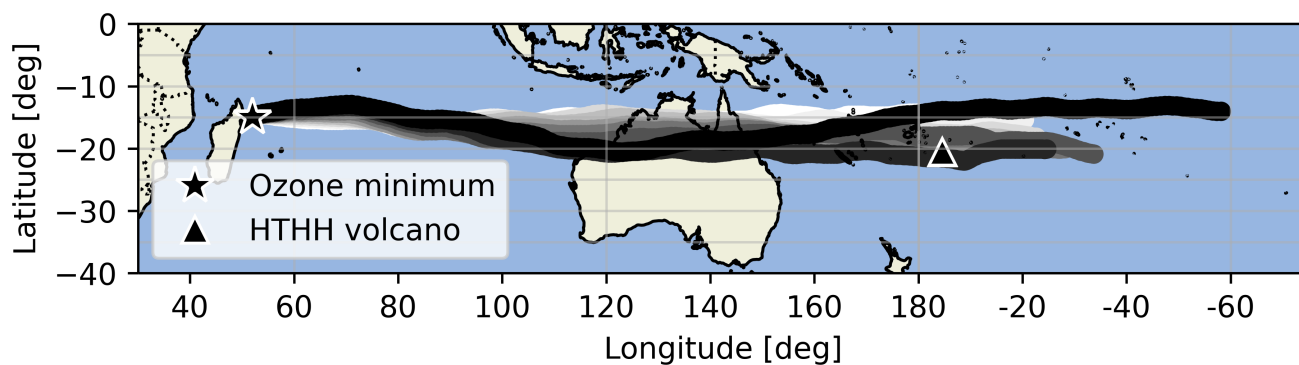


Figure 8. HYSPLIT back-trajectories of 240 hours ending on 22 January at 03:00 UTC at the minimum of total ozone near Madagascar, between 22 and 26 km height. The star and triangle symbols indicate the ending point and the HTHH volcano location, respectively. The back-trajectories are displayed with thick lines of different shades of grey, ranging from white for the 22 km height to black for 26 km.

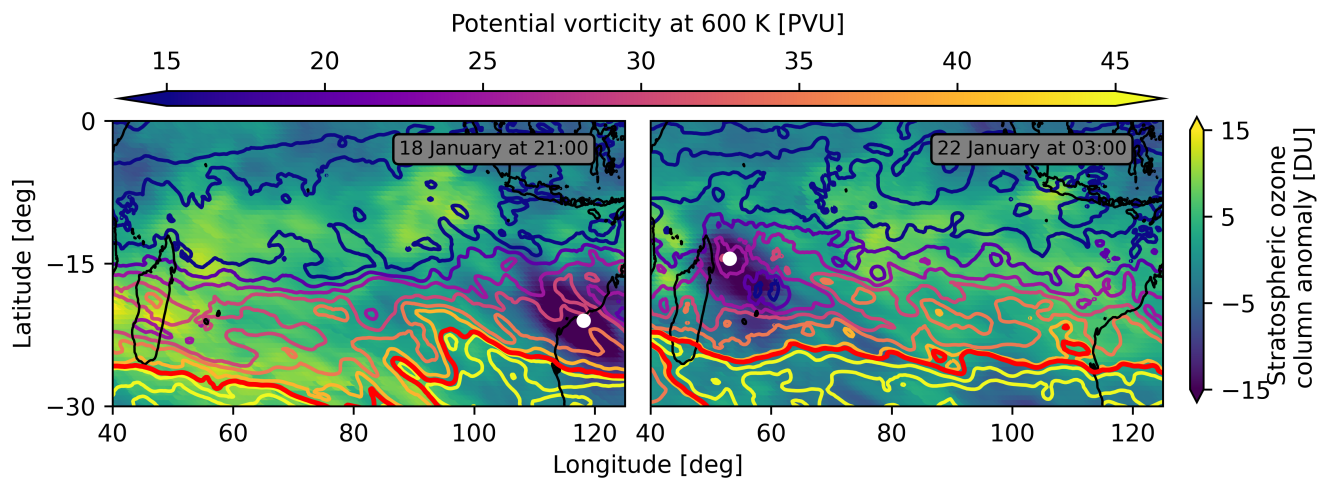


Figure 9. Instantaneous stratospheric ozone column anomaly maps and contours of the ERA5 hemispheric EPV for 18 January at 21:00 UTC and 22 January at 03:00 UTC. The red thick line represents the DYBAL estimated position of the subtropical barrier and the white dot symbols indicate the positions of stratospheric ozone minima.